



Society of Petroleum Engineers

SPE-217771-MS

Practical Optimization of Perforation Design with a General Correlation for Proppant and Slurry Transport from the Wellbore

Egor Dontsov and Christopher Ponnors, ResFrac Corporation, Palo Alto, CA, USA; Kevin Torbert, Cornerstone Engineering, Inc., Bakersfield, CA, USA; Mark McClure, ResFrac Corporation, Palo Alto, CA, USA

Copyright 2024, Society of Petroleum Engineers DOI [10.2118/217771-MS](https://doi.org/10.2118/217771-MS)

This paper was prepared for presentation at the SPE Hydraulic Fracturing Technology Conference and Exhibition, The Woodlands, Texas, USA, 6 - 8 February 2024.

This paper was selected for presentation by an SPE program committee following review of information contained in an abstract submitted by the author(s). Contents of the paper have not been reviewed by the Society of Petroleum Engineers and are subject to correction by the author(s). The material does not necessarily reflect any position of the Society of Petroleum Engineers, its officers, or members. Electronic reproduction, distribution, or storage of any part of this paper without the written consent of the Society of Petroleum Engineers is prohibited. Permission to reproduce in print is restricted to an abstract of not more than 300 words; illustrations may not be copied. The abstract must contain conspicuous acknowledgment of SPE copyright.

Abstract

During plug and perf completion, perforation pressure drop is used to encourage a uniform distribution of flow between clusters by overcoming stress shadowing, stress variability, and nonuniform breakdown pressure. However, proppant inertia, gravitational settling, and perforation erosion contribute to nonuniformity, even with an aggressive limited-entry design. In prior work, [Dontsov \(2023\)](#) developed a correlation for predicting proppant outflow from the wellbore as a function of slurry velocity, perforation phasing, and other parameters. In the present study, the [Dontsov \(2023\)](#) correlation is integrated into a wellbore dynamics simulator capturing key physical processes that control slurry and proppant outflow from the wellbore, such as erosion, stress shadowing, and near-wellbore tortuosity. The simulator is fast running and incorporated into a tool for Monte Carlo uncertainty quantification and design optimization. First, we run a series of sensitivity analysis simulations to evaluate the effect of key model inputs. The simulations demonstrate processes that can cause heel bias, toe bias, or heel/toe bias in the erosion distribution. Next, we apply the tool to analyze field datasets from the Eagle Ford and the Montney. Downhole imaging of erosion data enables model calibration. Calibration is necessary because differences in casing, cement, and formation properties cause differences in erosion behavior and flow distribution. Parameters controlling the magnitude of erosion and stress shadow are modified to match the trends observed from the downhole imaging. After calibration is performed, the model is applied to maximize the uniformity of proppant placement by optimizing perforation phasing, diameter, count, and cluster spacing.

Introduction

Optimizing uniformity is the key to maximizing recovery in shale plays. Uneven fracture and proppant placement results in gaps between depleting fractures, and as a result, regions of relatively undrained rock ([Raterman et al., 2019](#); [Kaufman et al., 2019](#)). The goal of maximizing uniformity has led companies to adopt cluster spacing in the range of 10-40 ft, much tighter than the designs used in the earlier years of the shale revolution ([Xiong, 2020](#)).

Designs with tighter spacing have been successful in increasing recovery. However, tighter cluster spacing increases fracture-to-fracture stress shadowing, which brings an array of challenges: (a) greater

irregularity of fracture geometry (Dontsov and Suarez-Rivera, 2020; McClure et al., 2020); (b) more height growth out of zone (Dohmen et al., 2014); and (c) greater difficulty achieving flow uniformity between clusters, especially with larger numbers of clusters per stage (Dhuldhoya and Frieauf, 2022). Some of these effects are unavoidable and must be considered as part of global optimization of design (McClure et al., 2023a). On the other hand, the effect on uniformity of flow can be substantially mitigated with limited-entry completion (Lecampion et al., 2015; Weddle et al., 2018; Cramer et al., 2020; Lorwongngam et al., 2023). However, because of inertial and gravitational effects, proppant flow from the wellbore can be nonuniform *even if slurry flow is relatively uniform* (Wu and Sharma, 2016; Snider et al., 2022). Even if slurry is uniform at the beginning of a stage, erosion caused by proppant flow may be nonuniform, reducing the uniformity of slurry flow as the pumping progresses.

Because of the challenges created by proppant dynamics, ‘increasing limited-entry’ is not a panacea for maximizing uniformity. Limited-entry is a critical component of modern fracturing design, but perforation erosion, proppant inertia, and gravitational effects interact to create complex phenomena that cause non-uniformity, even with high perforation pressure drop.

There has been significant progress in the literature in understanding proppant transport from the wellbore (Gruesbeck and Collins, 1982; Gillies, 1993; Wu and Sharma, 2016; Ngameni et al., 2017; Wu, 2018; Ahmad and Miskimins, 2019a; Ahmad and Miskimins, 2019b; Ahmad, 2020; Ahmad et al., 2021; Liu et al., 2021; Snider et al., 2022; Wang et al., 2022). However, literature studies have generally provided results specific to a particular set of circumstances, without providing a general-purpose correlation that can be applied for simulation and optimization. To address this limitation, Dontsov (2023) synthesized the literature and derived a general correlation for predicting proppant transport from the wellbore as a function of slurry velocity, fluid properties, proppant type and concentration, wellbore diameter, perforation phasing and diameter, etc. The correlation was validated by comparison with a wide range of published results.

To apply the Dontsov (2023) correlation for practical perforation design optimization, it needs to be embedded inside a broader simulator that incorporates the key physics that affect fluid/slurry distribution, including: (a) perforation pressure drop, (b) near-wellbore tortuosity, (c) fracture-to-fracture and stage-to-stage stress shadow, (d) heterogeneity of stress, and (e) perforation erosion. In addition, practical causes of non-ideality must be considered: (a) random variability in perforation phasing and diameter, (b) perforation diameter dependence on phasing, (c) perforation plugging, and (d) variability in breakdown pressure between clusters.

In this paper, we describe the implementation and application of a wellbore dynamics simulator that incorporates the Dontsov (2023) correlation and the other key physical processes required to describe proppant and slurry flow from the wellbore. The tool is fast running, able to perform a large number of simulations for Monte Carlo uncertainty quantification within a few seconds.

The tool does not include a fracture propagation algorithm or reservoir simulation capability. Therefore, it is not capable of solving general fracture design optimization problems, which require consideration of the full set of interactions between design variables, formation properties, well spacing, production, and overall project economics. Instead, the tool is designed to quickly and practically solve a narrower problem – optimization of perforation cluster design to maximize the uniformity of slurry and proppant flow from the wellbore. In future work, we will describe implementation of the Dontsov (2023) correlations inside of a much more general hydraulic fracturing and reservoir simulator (McClure et al., 2023b).

Methods

Practical engineering workflow

The workflow for optimizing perforation design synthesizes: (a) a wellbore dynamics simulator, and (b) empirical observation of field-scale phenomena. The calculations utilize a handful of fitting parameters that can be assessed from comparison with field data. Generic baseline values can be used for the fitting

parameters, if necessary, but accuracy can be improved by calibrating to field observations. Fortunately, calibration data for the workflow is readily available – downhole imaging technologies provide cost-effective and high-fidelity assessments of the magnitude and location of perforation erosion within a stage (Cramer et al., 2020; Robinson et al., 2020). This data can be incorporated into a practical process for model calibration and design optimization.

The recommended workflow is:

1. Identify project objectives. Which perforation design parameters will be considered for modification as part of an optimization workflow? These may include phasing, diameter, shot count for each cluster, stage length, and cluster spacing.
2. Identify datasets for calibration. Select one or more datasets from wells that have been analyzed with downhole imaging of post-job perforation diameter.
 - a. The model calibration will seek a single set of parameters that provide a ‘best possible’ match to the available data. Therefore, the calibration datasets should be taken from wells that are considered ‘comparable’ to one another, and comparable to the upcoming wells that the model will be used to optimize. Wells may not be ‘comparable’ if they are from different geologic basins or employ different types of casing, for example. On the other hand, stages that vary in cluster design parameters such as phasing or shot count can be considered ‘comparable.’ In fact, data with a variety of cluster designs can be useful for calibration. The decision on which datasets to consider ‘comparable’ is subjective and requires engineering judgement.
 - b. If downhole imaging data is not available, then it is acceptable to use default calibration parameters as a starting point.
3. Statistically summarize the observations from the field datasets.
 - a. What is the systematic random variance in perforation phasing (on both a ‘per stage’ and ‘per shot’ basis)? Based on calibration shots, what is the random variance in the initial (pre-job) diameter?
 - b. Each discrete ‘design’ is characterized by a particular choice of phasing, shot count, etc. For each design, what are the median and P10/P90 erosion (increase in area or effective diameter) observed for each shot? Matching this trend is a key objective for the calibration.
 - c. Assess confidence in the observations – what is the sample size? Field data exhibits considerable variability from stage-to-stage; it is best to aggregate observations from at least 5-10 stages per design, and ideally more. If there are fewer than five stages available for a particular design, utilize the results with caution.
4. Vary model input parameters to match the observed erosion data. The main parameters that should be varied for calibration are described in Section 3.1.1.
 - a. If the field data includes stages using different designs (for example, different shot counts per cluster or cluster counts per stage), seek a single set of calibration parameters that does the best job of simultaneously matching the trends seen with all the designs.
 - b. Sometimes, it may be necessary to use different calibration parameters to match data from different wells, even if they are landed in the same zone. If so, do your best to explain why the observations are different and develop hypotheses that may explain any differences.
 - c. If the gathered data between wells appears mutually inconsistent and unexplainable (i.e., two wells that superficially appear comparable exhibit distinctly different trends in the data), then engineering judgment must be used to assess which set of observations should be considered the ‘ground truth’ for purposes of model calibration.
5. Optimize cluster design.

- After the calibration is complete, vary design parameters such as phasing, shot count per stage, and initial diameter to identify the design that maximizes the uniformity index of proppant and/or slurry.
- The wellbore dynamics simulator reports the uniformity index on a ‘per cluster’ basis and a ‘per shot’ basis. Usually, the ‘per cluster’ uniformity is the metric that should be optimized, since we commonly assume that the slurry that flows into each shot in a cluster comes in from outside the casing.

In most shale wells, the same cluster design is used in every stage along a well. Thus, we will seek a single ‘optimal’ cluster design to apply uniformly along a well. However, some operators have reported positive results from optimizing each individual stage. For example, [Mientka et al. \(2018\)](#) use drilling data to estimate the variation in stress along a horizontal lateral, and then optimize stage placement to fracture ‘like with like.’ Because it is fast running, the tool can be readily applied for this type of workflow, quickly generating an optimal design for each stage along a lateral.

Implementation of the wellbore dynamics simulator

The wellbore dynamics simulator performs a series of timesteps. In each timestep, it calculates the slurry and proppant outflow from each perforation. Between timesteps, it updates perforation erosion, checks for fracture initiation, and applies checks for perforation plugging.

Slurry exits the well through a series of perforation clusters, each of which contains one or more perforation holes (or shots). At each cluster, slurry outflow and fracture initiation are affected by the ‘external’ stress shadow from prior stages, as well as the ‘internal’ stress shadow from fractures propagating within the same stage. Panels (a) and (c) from [Figure 1](#) schematically shows an example with two propagating fractures within a stage, and ‘external’ stress shadow from the prior stage. The stress shadow from the prior stage and from the two fractures within the stage superimpose to determine the stress at each cluster.

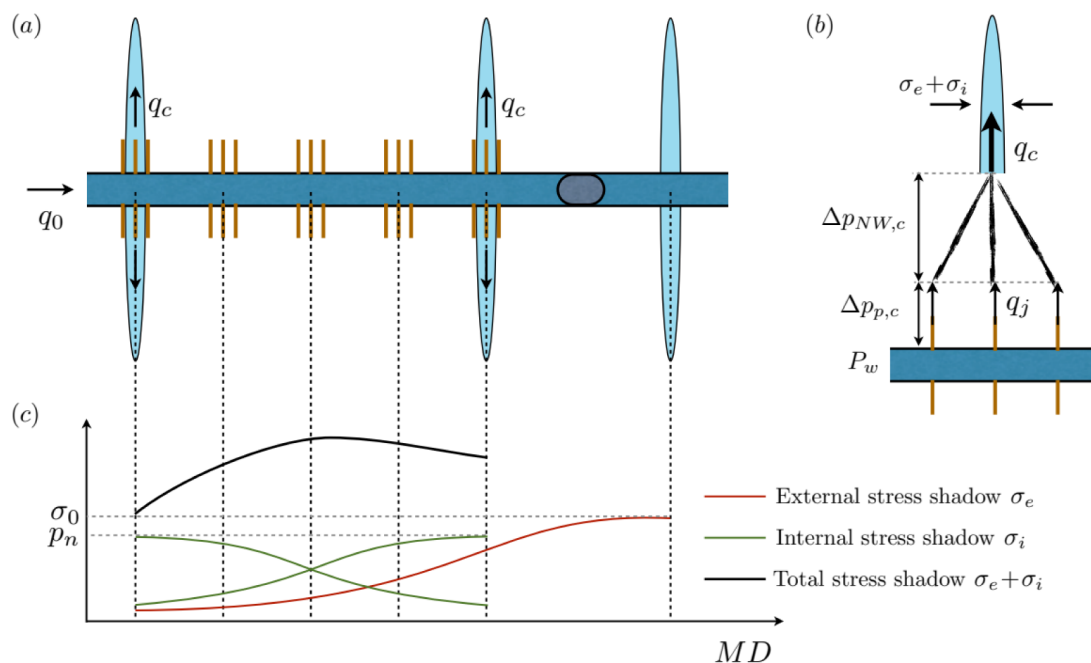


Figure 1—Panel (a): Schematics of initiated fractures from the stage together with the external fracture. Panel (b): Distribution of pressure drops from the wellbore to the fracture for a given cluster. Panel (c): Example stress shadow calculation from both internal and external fractures.

For fracture initiation, every perforation is assigned a value of effective tensile strength. As soon as pressure in the wellbore exceeds the minimum principal stress by the effective tensile strength, a fracture initiates. The initiation condition at perforation c is written as:

$$P_w > T_{str,eff,c} + \Delta\sigma_{e,c} + \Delta\sigma_{i,c} + \sigma_{init,c}, \quad (1)$$

where P_w is the pressure in the wellbore, $T_{str,eff,c}$ is the effective tensile strength, $\Delta\sigma_{e,c}$ is the stress shadow from the prior stage, $\Delta\sigma_{i,c}$ is the stress shadow from other fractures within the same stage, and $\sigma_{init,c}$ is the initial magnitude of the minimum principal stress at the cluster. The values of $\Delta\sigma_{e,c}$, $T_{str,eff,c}$, and $\sigma_{init,c}$ are specified by the user for each cluster and do not change over time during the calculation. The user can optionally specify that $T_{str,eff,c}$ has random variability according to a normal distribution with a specified mean and standard deviation. The external stress shadow $\Delta\sigma_{e,c}$ is individually specified for each cluster. The most common approach is to specify the ‘maximum stress shadow from the prior stage,’ and then apply the Sneddon solution to calculate the decay in stress shadow with distance, which allows the user to quickly assign a spatially variable value of $\Delta\sigma_{e,c}$ at each cluster.

The internal stress shadow $\Delta\sigma_{i,c}$ is calculated adaptively during the simulation. The user specifies a ‘fracture net pressure.’ If only a single fracture has initiated, the value of $\Delta\sigma_{i,c}$ is equal to the user-specified net pressure. Assuming a constant height fracture, the Sneddon solution is used to calculate the stress shadow and its effect on $\Delta\sigma_{i,c}$ at the neighboring perforations. With an array of propagating fractures, the ‘internal’ stress shadow at each cluster is the superposition of the stress shadow from all other propagating fractures within the stage.

The slurry flow rate in each cluster is calculated accounting for perforation friction, stress shadow, and near-wellbore tortuosity. In each timestep, the solver finds the value of wellbore pressure, P_w , such that the sum of the flow rate from each cluster q_c , equals the specified injection rate, q_0 :

$$\sum_{(c=1)}^N q_c = q_0 \quad (2)$$

It is assumed that each cluster is exposed to the same wellbore pressure everywhere along the stage (i.e., frictional pressure drop along the lateral within the stage is neglected). For a given value P_w , the flow rate at each cluster is calculated by solving the following nonlinear equation for q_c :

$$P_w = \Delta p_{p,c}(q_c) + \Delta p_{NW,c}(q_c) + \Delta\sigma_{e,c} + \Delta\sigma_{i,c} + \sigma_{init,c}, \quad (3)$$

where $\Delta p_{p,c}(q_c)$ is perforation pressure drop for the cluster and $\Delta p_{NW,c}(q_c)$ is the near-wellbore pressure drop.

The near-wellbore pressure drop is calculated as:

$$\Delta p_{NW,c}(q_c) = A_{NW,c} q_c^{n_c}, \quad (4)$$

where $A_{NW,c}$ is the specified near-wellbore pressure drop coefficient and n_c is the near-wellbore pressure drop exponent.

The perforation pressure drop is the same for each shot within a cluster. However, shots can have different diameters, and so the flow rate varies between the perforations in each cluster. The flow rate through each shot j is determined from the expression for perforation pressure drop. Written in field units (provided in the nomenclature), the equation for perforation pressure drop is (Cramer, 1987):

$$\Delta p_{p,j} = 0.2369 \frac{\rho_f q_j^2}{C_{d,j}^2 D_j^4}, \quad (5)$$

where q_j is the flow rate through j th perforation shot, ρ_f is the fluid density, $C_{d,j}$ is discharge coefficient, and D_j is effective perforation diameter.

The overall flow rate through the cluster c is calculated as the sum of the flow rates through each shot in the cluster:

$$\sum_{j=1}^{N_c} q_j = q_c \quad (6)$$

The distribution of proppant that flows into each shot depends on three primary physical phenomena: (a) the distribution of slurry that flows into each shot, (b) proppant settling in the wellbore, and (c) proppant turning efficiency. Both particle settling and turning are described in detail by [Dontsov \(2023\)](#). The [Dontsov \(2023\)](#) model is calibrated against numerous laboratory scale, field scale, and computational experiments, such as: [Gillies \(1993\)](#), [Ngameni et al. \(2017\)](#), [Ahmad and Miskimins \(2019\)](#), [Ahmad and Miskimins \(2021\)](#), [Wu and Sharma \(2016\)](#), [Wu and Sharma \(2019\)](#), [Snider et al. \(2022\)](#), [Liu et al. \(2021\)](#), and [Wang et al. \(2022\)](#).

Particle turning can be characterized with the metric ‘turning efficiency,’ which is defined as the proppant concentration flowing through a perforation shot divided by the average proppant concentration in the wellbore at the location of the shot. Turning efficiency primarily depends on particle size, and it usually varies between 0.7 to 0.9.

As the flow rate in the wellbore decreases from heel to toe, the ability of fluid to suspend particles reduces. Thus, toe clusters are typically more affected by particle settling than the heel clusters.

[Figure 2\(a\)](#) shows a wellbore cross-section and schematically shows non-uniform particle distribution caused by settling. The fluid and proppant ‘ingestion zones’ are the regions of the cross-sectional area in the well that flow into a particular perforation shot. In the ideal case of uniform velocity distribution within the cross-section, the area of the fluid ingestion zone (outlined by the dashed blue line) relative to the area of the wellbore's cross-section is equal to the slurry flow rate through the perforation divided by the total flow rate through the wellbore (immediately upstream from the perforation). In reality, the velocity distribution across the cross-sectional diameter is non-uniform, which affects the size of the ingestion region. The nonuniformity of flow is considered by the full [Dontsov \(2023\)](#) correlation, but for simplicity, in the present discussion, we assume uniform velocity distribution. For typical parameters, the ratio of ingestion zone area to cross-sectional area is often small. As a hypothetical example, let's assume 10 clusters with 3 perforations per cluster at 120° phasing, 90 bpm injection rate, and that the flow rate per shot is uniform. At the heel-most perforation, the ratio of flow rate per shot to total flow rate will be $3/90 = 0.033$. At the last cluster, this ratio will be $3/9 = 0.33$. Comparing proppant ingestion and fluid ingestion, the area associated with proppant ingestion is smaller by an amount determined by the turning efficiency (which implies a reduction of approximately 10-30%).

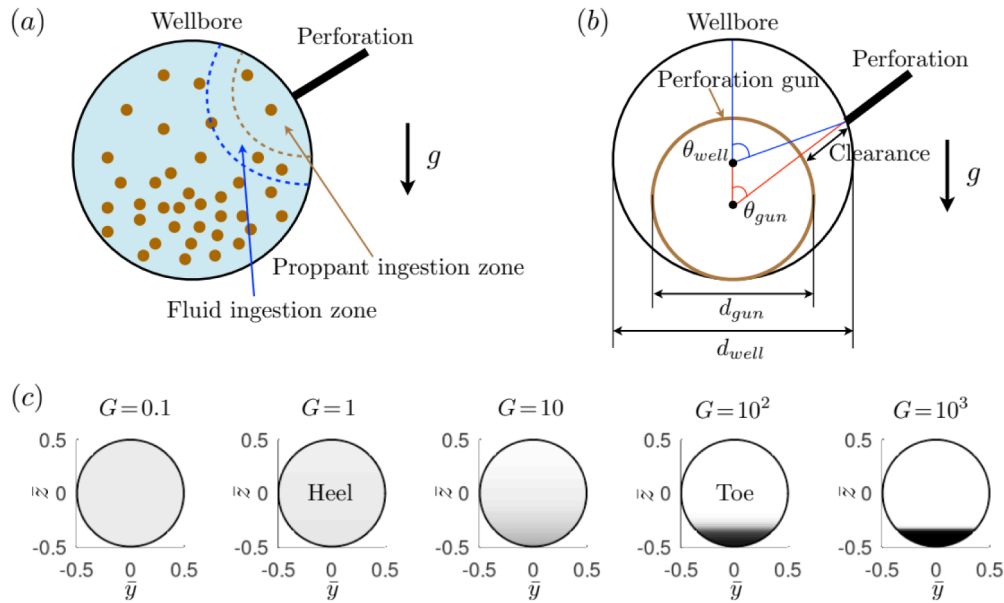


Figure 2—Panel (a): Slurry flow in the wellbore cross-section with particle settling. Fluid and proppant ingestion zones are shown by the dashed lines. Panel (b): Schematics for wellbore versus perforation gun centered azimuths. Panel (c): Particle concentration in the wellbore for different values of the dimensionless gravity G . Figure is reproduced from [Dontsov et al. \(2023b\)](#).

The size of the ingestion zone affects proppant outflow from the well because the distribution of proppant is not uniform across the cross-sectional area. As an example, let's consider a perforation shot located at the top of the well, close to the toe of the stage. Because of the settling of proppant towards the bottom of the well as slurry velocity drops towards the toe, the average proppant concentration in the proppant ingestion zone for the shot (at the top of the well) is significantly lower than the average proppant concentration across the full cross-sectional area. This reduces the amount of proppant exiting the well from that shot. Thus, the effect of perforation phasing becomes crucial when there is a substantial particle settling because the amount of proppant that enters the perforation depends on particle concentration in the local region around the perforation.

To quantify particle settling, [Dontsov \(2023\)](#) defined a parameter G , for dimensionless gravity. [Figure 2\(c\)](#) shows the particle volume fraction distribution in the well for different values of G . Writing the equation in S.I. units (not field units), the parameter G is defined as:

$$G = \frac{8\phi_m(\rho_p - \rho_f)g\cos(\theta_w)d_{well}}{f_D\rho_f v_w^2}, \quad (7)$$

where $\phi_m = 0.585$ is the maximum flowing volume fraction of particles, ρ_p is particle mass density, ρ_f is fluid mass density, $g = 9.81 \text{ m/s}^2$ is gravitational constant, d_{well} is wellbore diameter, $f_D = 0.04$ is a fitting parameter that can also be interpreted as a friction factor in the pipe, and v_w is the average wellbore velocity or the total wellbore flow rate divided by the cross-sectional area. To account for dipping wells, the dip angle θ_w can be introduced. For horizontal wells $\theta_w = 0$. The only parameter that changes along the stage is the average wellbore velocity. For heel perforations, the velocity is high and the value of the parameter G is low (on the order of 1 for typical parameters). This leads to nearly uniform proppant distribution, as shown in [Figure 2\(c\)](#). At the same time, velocity is much lower for toe perforations and the dimensionless gravity G can exceed 100. This results in significantly asymmetric particle distribution, in which particle flow resembles a 'flowing bed' state, such as shown in [Figure 2\(c\)](#).

[Figure 2\(b\)](#) illustrates how the perforation gun diameter is often noticeably smaller than the inner wellbore diameter. Therefore, the perforation azimuth relative to the center of the well θ_{well} and the corresponding

azimuth relative to the center of the gun θ_{gun} are different. This causes the actual shot azimuth within the well – which is what actually affects the proppant distribution – to be different from the phasing ‘specified’ as part of the design. If the ratio between the perforation gun and wellbore diameters is known, the value of θ_{well} can be calculated from θ_{gun} :

$$\theta_{well} = \theta_{gun} + \sin^{-1}(\sin(\theta_{gun})), \quad \theta_{gun} = \tan^{-1}\left(\left(r + \cos(\theta_{well})\right)^{-1} \sin(\theta_{well})\right), \quad r = 1 - \frac{d_{gun}}{d_{well}}. \quad (8)$$

Perforation diameter depends on the perforation gun clearance, which is defined in Figure 2(b). The bigger the clearance, the smaller the resultant hole diameter. The simulator incorporates this effect when setting up the initial perforation diameters at the beginning of the simulation. Figure 3 shows the relation that is used to adjust perforation diameter as a function of gun clearance (and implicitly, as a function of phasing). The curve is based on a fit to field data from Bell et al. (1995). For a particular value of casing diameter and gun diameter, the right panel in Figure 3 shows the normalized perforation diameter versus θ_{gun} .

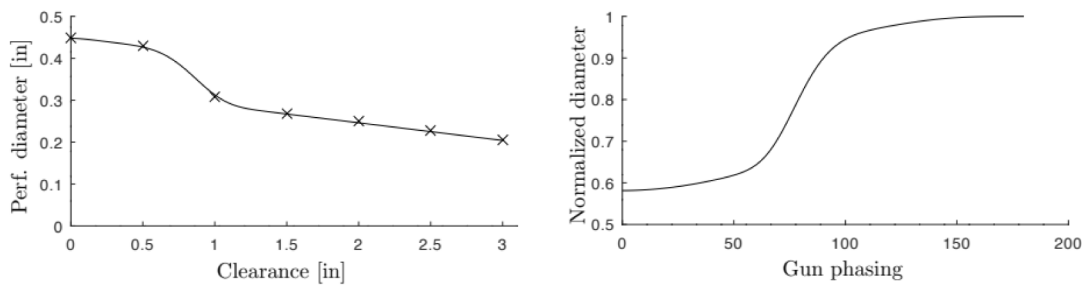


Figure 3—Left Panel: Perforation diameter versus clearance. Right Panel: Calculated normalized diameter versus gun phasing.

To derive a general correlation, the data from Bell et al. (1995) is fit by a model curve (the solid line on the left panel). For a particular configuration, the gun clearance can be calculated from wellbore diameter, gun diameter, and phasing. Then, the curve fit is used to calculate the ‘normalized diameter’ shown on the right panel of Figure 3. The actual initial perforation diameter is calculated by multiplying the designed diameter by the ‘normalized diameter.’

Based on calibration shots from a specific project, the user may assess that the effect of clearance on diameter is greater or smaller than shown in Figure 3. To adjust, the user is permitted to specify a multiplier that weakens or strengthens the effect of clearance on diameter. If the multiplier is set to zero, then clearance has no effect; if the multiplier is set to 0.5, then the effect on diameter is 50% weaker than shown in Figure 3; and if the multiplier is set to 1.0, then the curve shown in Figure 3 is used directly.

Field observations with downhole camera demonstrate that perforations are sometimes screened out by proppant at the end of the treatment. To model this phenomenon, a simple model is adopted. The probability of perforation screen-out is proportional to the total mass of proppant that flows through each perforation shot. This assumption is likely an oversimplification, and in ongoing work, we are evaluating alternatives. In addition, a plugging bias is introduced to account for the fact that perforations that are located at the bottom of the well have a higher chance of being plugged. While ‘perforation plugging’ assessments are commonly available from downhole imaging analyses, care should be taken when using these interpretations, because it is possible for perforations to plug after shut-in.

Perforation erosion has a major effect because it causes the flow distribution to evolve over time. Cramer (1987) posited that, after an initial ‘rounding’ period, erosion should scale linearly with the volume of proppant that flows through each shot. Long et al. (2015) proposed a slightly different model, in which erosion scales with the square of the average velocity of flow through the shot. In the present work, we utilize a modified version of the Long et al. (2015) model. In ongoing work, we are evaluating different

potential erosion models – including both the Cramer (1987) and Long et al. (2015) models – to assess which provides the best consistency with field data.

We extend the Long et al. (2015) erosion model to include the effect of lateral fluid velocity on erosion. It is usually observed that heel-side perforations erode preferentially (despite the inertial effect that causes proppant to flow past the perforations), and it is also observed that perforations erode predominantly in the downstream direction of the fluid flow (Cramer et al., 2020). To capture this behavior, we modify the erosion model Long et al. (2015) as:

$$\frac{dD_u}{dt} = \alpha C v_p^2, \quad \frac{dD_s}{dt} = \alpha C v_p^2, \quad \frac{dD_d}{dt} = \alpha C (v_p^2 + \gamma v_w^2), \quad \frac{dC_d}{dt} = \beta C v_p^2 \left(1 - \frac{C_d}{C_{d,max}}\right), \quad (9)$$

where D_u is the effective diameter in the upstream direction, D_s is the diameter in the direction perpendicular to fluid flow, D_d is the downstream diameter, α is a fitting constant related to diameter erosion, β is a fitting parameter related to erosion of the coefficient of discharge, γ is a fitting parameter related to erosion related to lateral fluid velocity, C_d is the coefficient of discharge, $C_{d,max}$ is the maximum possible value of coefficient of discharge, C is proppant concentration (mass per volume), v_p is the superficial velocity through the shot (volumetric flow rate divided by cross-sectional area), v_w is the superficial velocity through the wellbore (volumetric flow rate divided by cross-sectional area), and t is time.

A schematic of an eroded perforation is shown in Figure 4. The eroded shape is a combination of a circular part in the upstream direction and an elliptical part in the downstream direction. The erosion in the downstream direction is affected by a term that is proportional to γ , which is a dimensionless parameter, as well as the squared superficial fluid velocity in the wellbore v_w (i.e., volumetric velocity divided by cross-sectional area). The gamma term introduces a heel bias in perforation erosion because the fluid velocity in the wellbore is highest at the heel of the stage and lowest at the toe of the stage.

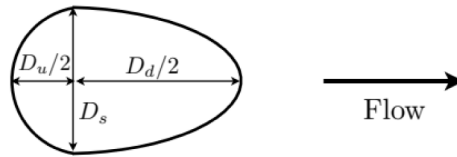


Figure 4—Schematic of an eroded perforation shot.

The values of α and β are calibrated in Long et al. (2015) based on the experimental results presented in Crump and Conway (1988). One issue is that the data was plotted on a logarithmic scale in Crump and Conway (1988), but it appears that the authors in Long et al. (2015) assumed a linear scale. This resulted in incorrect numeric values for the parameters α and β . With the corrected interpretation of the figure scale, the new values of the erosion parameters become: $\alpha = 3 \times 10^{-13} \text{ m}^2\text{s/kg}$, $\beta = 10^{-9} \text{ ms/kg}$.

In practical applications, we cannot always assume that the same value of α and β will be applicable in all cases. More angular proppant and thinner casing should lead to more erosion; conversely, rounder proppant and thicker casing should lead to less erosion. Casing steel quality, cement quality around the well, stress heterogeneity, and differences in near-wellbore tortuosity (caused stress state and rock properties) may also play a role.

To address the variability in practical observations, downhole imaging can be used to calibrate the model inputs to match available data. The β parameter is not a major source of uncertainty because in nearly all practical cases, the coefficient of discharge erodes rapidly to its maximum value close to one. However, the α and γ parameters can vary significantly between datasets (varying from 0.5 to 3x the baseline values, in our experience), and so it is beneficial to calibrate these parameters with field data.

For practical purposes, we define the values of α , β , and γ in terms of ‘multipliers’ from a default value. The default values of α and β are specified above. The default value of γ is set to be 100.

It is important to have an elongated perforation shape in the model because the ability of proppant to turn into perforation depends on the perforation size along the fluid flow direction, i.e. $(D_u + D_d)/2$. At the same time, perforation friction depends on the total area of the perforation. Therefore, it is useful to introduce the equivalent diameter as

$$D_{eq} = \sqrt{\frac{4A}{\pi}}, \quad A = \frac{\pi}{8} D_s (D_u + D_d). \quad (10)$$

In this case, the equation for perforation friction still holds if the equivalent diameter is used in it. Also, the circumferential and axial diameters, that are often reported in field data, are simply:

$$D_{cir} = D_s, \quad D_{ax} = \frac{1}{2}(D_u + D_d). \quad (11)$$

Note that in the model $D_s = D_u$, in which case there are only two independent diameters. Thus, the erosion model can be alternatively rewritten in terms of the circumferential and axial diameters as

$$\frac{dD_{cir}}{dt} = \alpha C v_p^2, \quad \frac{dD_{ax}}{dt} = \alpha C \left(v_p^2 + \frac{1}{2} \gamma v_w^2 \right), \quad \frac{dC_d}{dt} = \beta C v_p^2 \left(1 - \frac{C_d}{C_{d,max}} \right). \quad (12)$$

In this case, perforation area is $A = \pi D_{cir} D_{ax}/4$ and the equivalent diameter is $D_{eq} = \sqrt{D_{cir} D_{ax}}$

Proppant and slurry uniformity are often characterized by uniformity indices. The index can be calculated at the perforation level or at a cluster level. The indices are defined for the proppant and slurry as

$$U_p = 1 - \frac{\sqrt{\langle (m_p - \langle m_p \rangle)^2 \rangle}}{M \langle m_p \rangle}, \quad U_s = 1 - \frac{\sqrt{\langle (V_s - \langle V_s \rangle)^2 \rangle}}{M \langle V_s \rangle}. \quad (13)$$

Here $\langle \rangle$ represents the average operator, m_p is total proppant mass, while V_s is total slurry volume. The average is taken either over perforations or over clusters, depending on the type of uniformity index. The value of the multiplier $M=1$ for regular uniformity index, while it is taken as $M = \sqrt{N-1}$ for the normalized uniformity index, where N is either the number of perforations or the number of clusters (Wehunt et al., 2020).

Monte Carlo uncertainty quantification is used to assess the effect of the random variance in inputs parameters (Dontsov et al., 2023a; 2023b). A population of simulations is performed, making random draws from an uncertainty distribution for each stochastic parameter, and then the aggregated results are summarized statistically. Uncertainty is considered for: phasing on a stage level, phasing on an individual perforation level, individual perforation diameter, and effective tensile strength at each cluster. The stage level phasing uncertainty represents the variation of phasing from stage to stage, but not within the stage. For instance, if 0° phasing is specified and stage level uncertainty is 10° , then all perforations within the stage are assigned a phasing value between -10° and 10° for the case of uniform uncertainty. In contrast, if ‘normal’ uncertainty is selected, then the normal distribution with the standard deviation of 10° is applied to the base value. At the same time, the perforation level uncertainty assigns uncertainty for each individual perforation independently. In ongoing work, we are assessing whether additional causes of random variability should be included in the model's uncertainty quantification workflow.

The code also provides an algorithm for identifying the optimal perforation phasing (Dontsov et al., 2023a; 2023b). The algorithm accounts for uncertainty by maximizing the average uniformity index across a population of random draws.

Results and discussion

Sensitivity analysis simulations

Base Case simulation. A series of generic simulations were performed for sensitivity analysis. The parameters of the Base Case are shown in Table 1. The Base Case has ten clusters with two shots per cluster oriented at the top and at the bottom of the well. The injection schedule is shown in Figure 5. A clean fluid pad is followed by 90 bpm injection rate with a 100 mesh proppant ramp. Stress shadowing from the prior stage is fairly strong, with a maximum of 1500 psi at the toe of the stage and decaying with distance. The simulation includes a moderate degree of near-wellbore tortuosity, 200 psi/bpm^{0.5} for each cluster. The average ‘effective tensile stress’ at each cluster is 500 psi, with normally distributed random variability with standard deviation of 200 psi. The simulations have moderate random variability in phasing and perforation diameter.

Table 1—Parameters used in the Base Case for the sensitivity analysis. The primary parameters that may be varied as part of model calibration are shown in *italic* in the first eight rows on the right-hand side.

Parameter	Value	Parameter	Value
Stage length	200 ft	<i>Erosion alpha multiplier</i>	1
Casing inner diameter	4.8 inches	<i>Erosion gamma multiplier</i>	1
Perforation gun diameter	3.8 inches	<i>Probability of plugging multiplier</i>	1
Wellbore dip angle	0°	<i>Average effective tensile strength</i>	500 psi
Total fluid injection	6340 bbl	<i>Eff tensile strength uncertainty std</i>	200 psi
Total proppant injection	340,000 lbs	<i>Individual fracture net pressure</i>	200 psi
Designed phasing	0/180°	<i>Max stress shadow from prior stage</i>	1500 psi
Designed initial perf diameter	0.4 inches	<i>Near-wellbore tortuosity coefficient</i>	200 psi/bpm ^{0.5}
Initial discharge coefficient	0.9 (unitless)	Near-wellbore tortuosity exponent	0.5 (unitless)
Cluster spacing	20 ft	Perf phasing uncertainty std (stage)	20°
Proppant grain specific gravity	2.65 (unitless)	Perf phasing uncertainty std (individual)	20°
Proppant diameter	100 mesh	Perf diameter uncertainty std (individual)	0.03 inches
Fluid viscosity at 170 s ⁻¹	2 cp	Fluid power law index	0.85 (unitless)

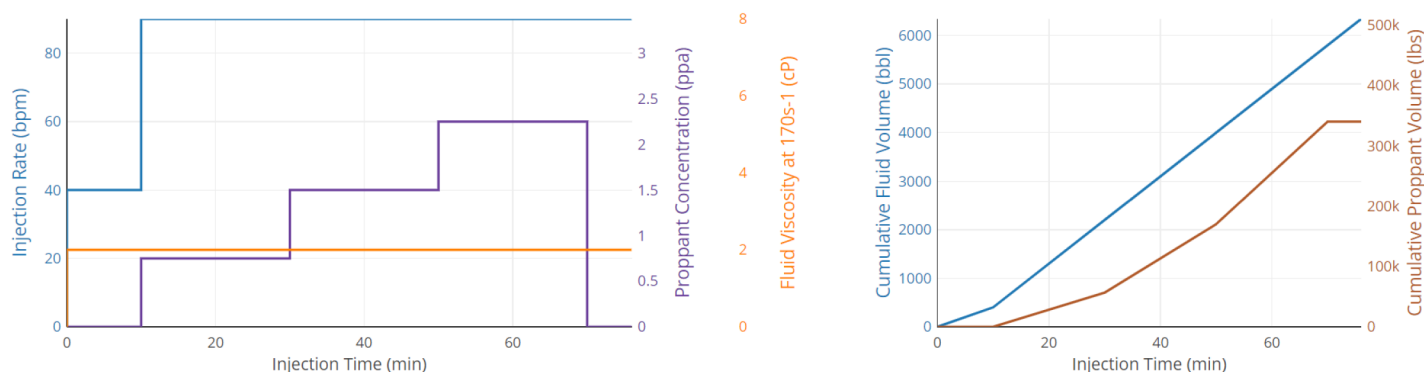


Figure 5—Injection schedule used in the Base Case.

The parameters that may be varied as part of model calibration are shown in *italic* in Table 1. They are the: ‘erosion alpha’ multiplier, ‘erosion gamma’ multiplier, ‘probability of plugging’ multiplier, average effective tensile strength, standard deviation in effective tensile strength, individual fracture net pressure,

‘maximum stress shadow from the prior stage’ (which decays with distance from the toe of the stage), and the near-wellbore tortuosity coefficient.

Figure 6 shows the initial and final perforation shots diameters from the Base Case simulation. Figure 7 shows the total proppant and slurry flow per shot and per cluster. Shots along the bottom of the well (180° phasing) have initial diameter of approximately 0.4 inches, which is equal to the ‘designed’ diameter. Because of the standoff from the gun to the top of the well, shots along the top of the well (0° phasing) have smaller initial diameter, 0.3 inches.

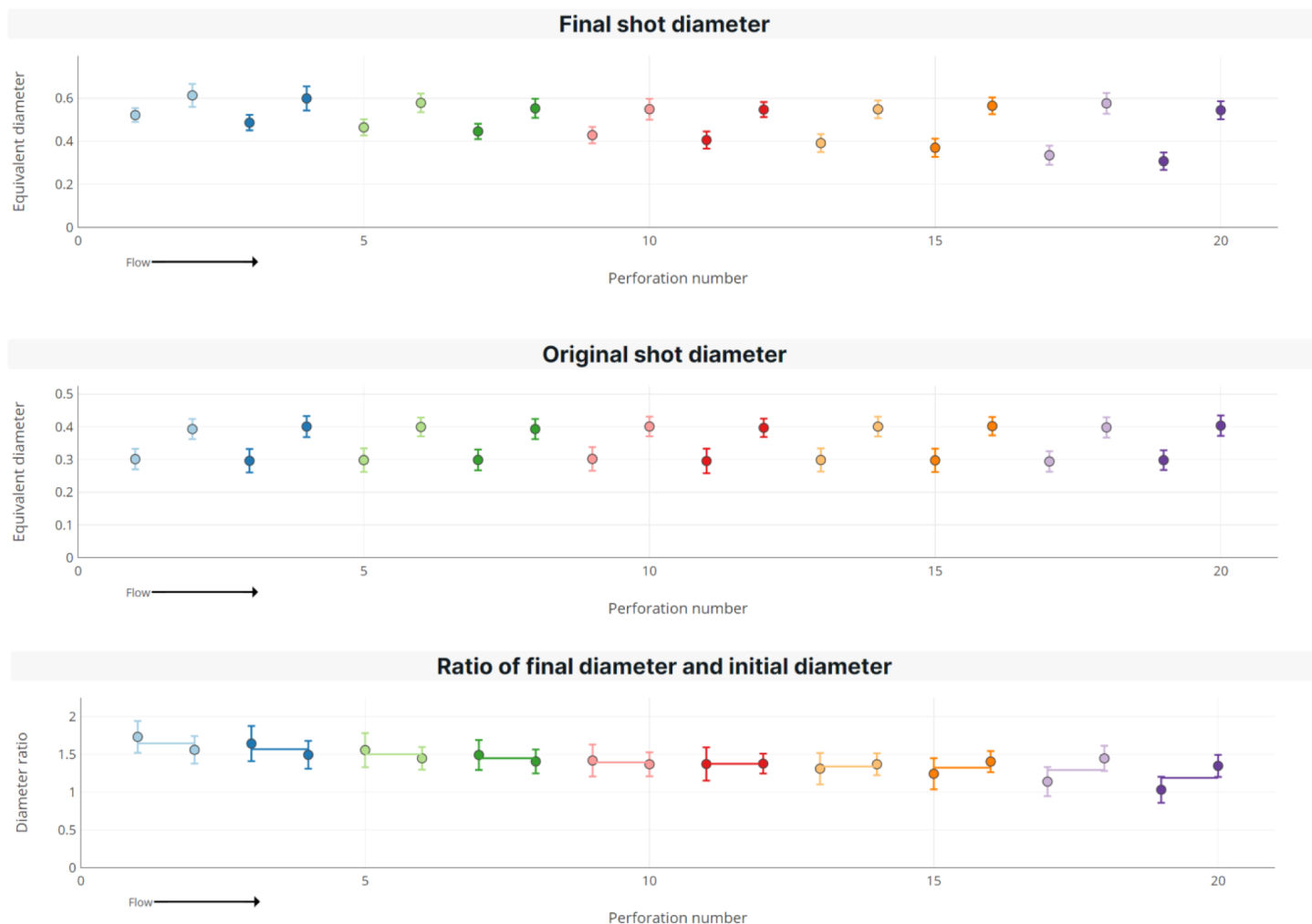


Figure 6—Initial perforation shot diameter, final shot diameter, the ratio of final to initial shot diameter in the Base Case.

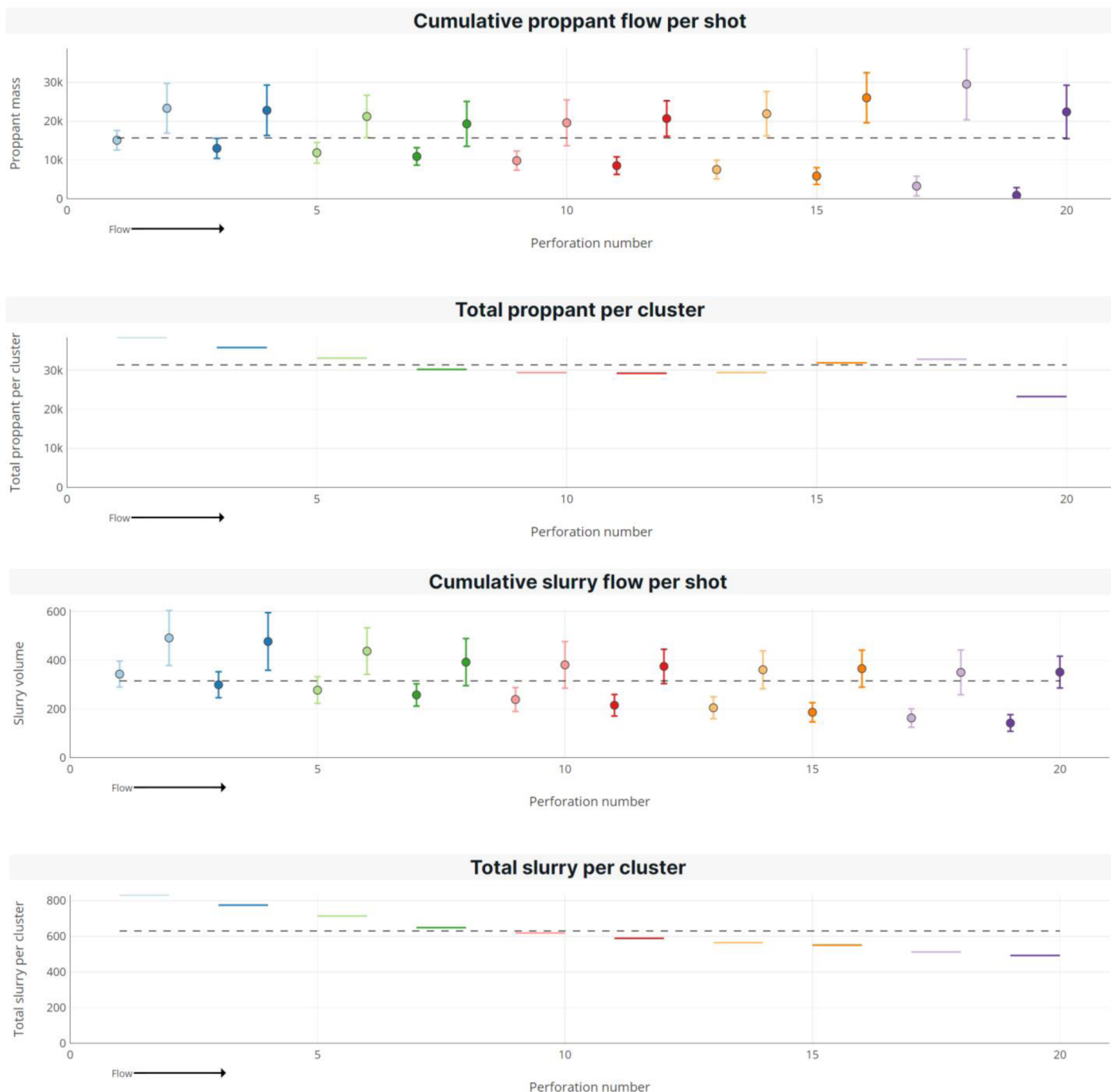


Figure 7—Cumulative proppant and slurry flow per shot and cluster in the Base Case.

Because of the horizontal velocity effect on erosion (Equation 9), Figure 6 shows that the clusters towards the heel experience proportionally more erosion than the clusters towards the toe.

The effect of phasing on erosion differs between the heel and toe sides of the stage. Towards the heel-side of the stage, Figure 6 indicates greater relative erosion in the shots along the top of the well. These shots start at a lower diameter, which reduces their flow rate and erosion, but because they start at lower diameter, they experience greater erosion on a proportional basis. Also, the Long et al. (2015) correlation predicts greater erosion with higher fluid velocities (Equation 9), which tends to accelerate erosion in smaller diameter holes. Conversely, towards the toe of the stage, the shots towards the bottom of the well experience greater erosion, relative to the shots at the top. As the slurry velocity decreases towards the toe, the proppant concentrates

towards the bottom of the well, causing more proppant to flow out of the lower-side shots. There is minimal proppant flow from the upper-side shots on the toe-side of the stage (Figure 7).

On a per-cluster basis, proppant outflow is relatively greater on the heel side. Inertial effects tend to cause proppant to bypass the heel clusters, which would seem to favor toe-bias. However, the difference in wellbore velocity causes erosion to be greatest on the heel side, which results in greater outflow of slurry on the heel side.

In the middle of the stage, as the proppant settles, the lower-side clusters disproportionately receive a higher proppant concentration, causing a gradual decrease in overall proppant concentration towards the toe. Because of this preferential outflow from the shots with 180° phasing, there is little proppant remaining by the time the slurry reaches the final cluster, and so it takes a disproportionately small volume of proppant. The high-side shot in the final perforation cluster receives almost zero proppant.

Figure 8 shows the initial and final ‘theoretical’ perforation pressure drop. The theoretical perforation pressure drop is calculated by assuming uniform flow rate into each shot and assuming that all shots will have diameter equal to the designed diameter. In the base case, all shots have the same designed diameter (0.4 inches), and so they all have the same initial ‘theoretical’ perforation pressure drop, 2000 psi. The ‘final’ theoretical perforation pressure drop is calculated by assuming that the flow rate is uniform into each shot but using the actual final diameters at the end of pumping. The next-to-last shot (top of the well) has a low initial diameter, and subsequently experiences little erosion. Therefore, its ‘final’ theoretical perforation pressure drop is very high – much higher than its initial ‘theoretical’ pressure drop (evaluated at the ‘designed’ diameter that is larger than the actual initial diameter). Most of the other clusters experience significant erosion and exhibit a final ‘theoretical’ pressure drop less than 1000 psi.

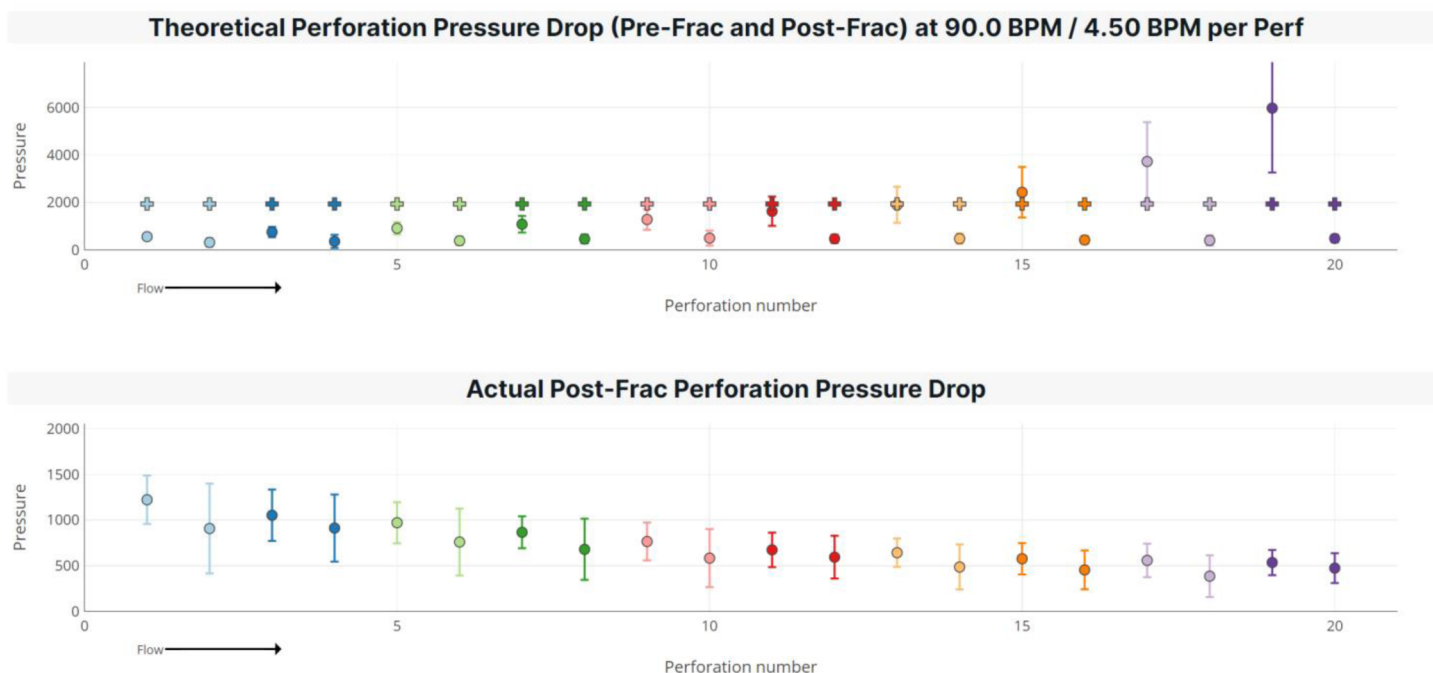


Figure 8—Initial and final theoretical perforation pressure drop, and the ‘true’ perforation pressure drop at the end of the stage.

The ‘actual post-frac perforation pressure drop’ plot outputs the ‘true’ perforation pressure drop across each shot, accounting for the variability in flow rate, stress shadow from the prior stage, and near-wellbore pressure drop. It shows a smooth variation, decreasing from around 1250 psi at the heel to around 500 psi at the toe. The ‘actual’ perforation pressure drop is very different from the ‘theoretical’ because the slurry flow rate is significantly different from shot to shot. Taking the second-to-last shot as an example, Figure 7 shows

that it has the least slurry flow of any shot. Therefore, even though it has the lowest final diameter and the largest ‘theoretical’ final perforation pressure drop, it has a relatively low ‘actual’ perforation pressure drop.

The decreasing trend from heel-to-toe in ‘actual’ post-frac perforation pressure drop occurs because of the greater stress shadow towards the toe side of the stage, which reduces flow rate towards the toe. Other factors that can affect the trend in ‘actual’ perforation pressure drop include: stress shadowing between fractures within the same stage (which tends to preferentially reduce flow along the middle of the stage), and variability in near-wellbore tortuosity between clusters (which is not applicable in this case, because tortuosity was set to be uniform).

Figure 9 shows histograms of the uniformity index and regularized uniformity index for 100 random realizations from the Monte Carlo uncertainty quantification.

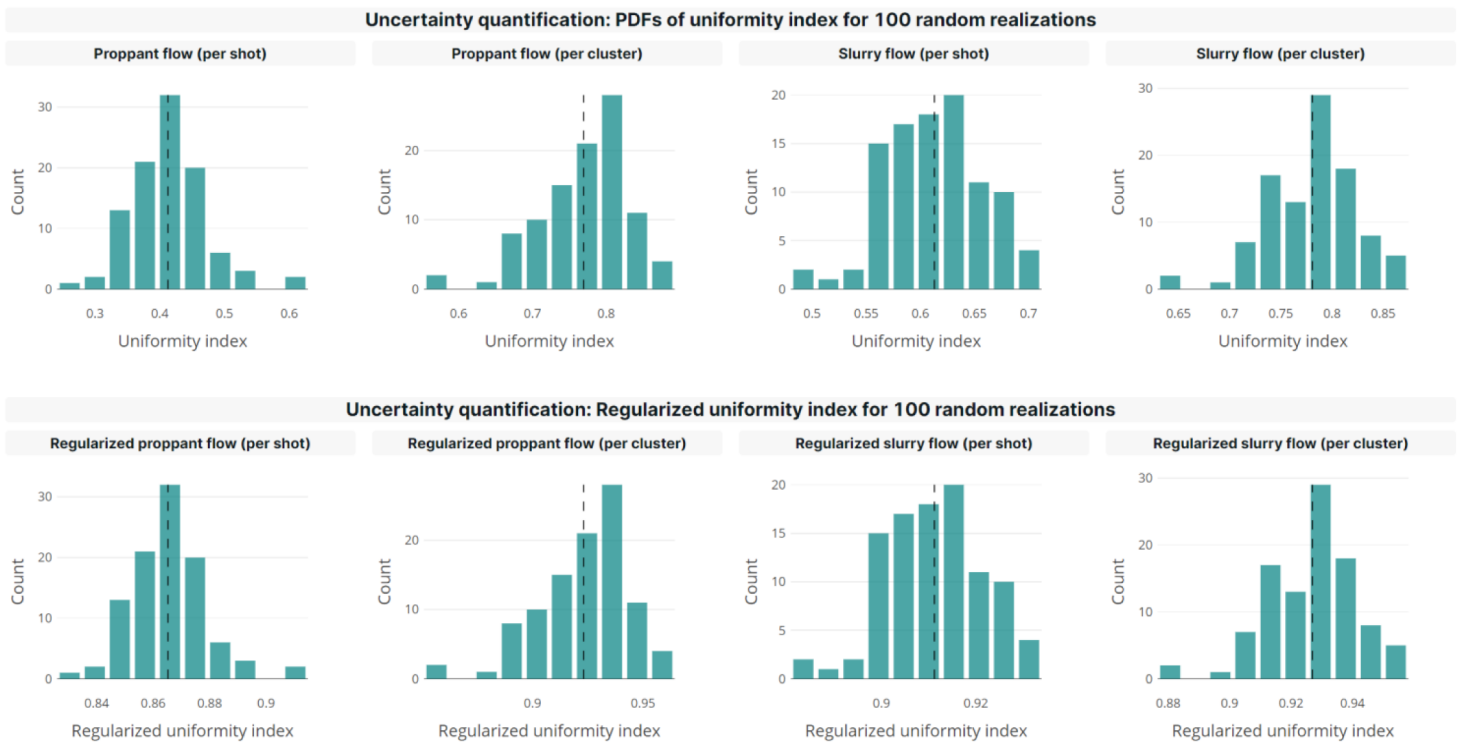


Figure 9—Histograms of uniformity index and regularized uniformity index for slurry and proppant flow per shot and per cluster.

Uniformity index is a measure of how evenly a quantity (either proppant or slurry) is distributed among an entity (clusters or perforation), as defined in Equation 13. The uniformity index has an upper bound of one, which would be a perfectly flat distribution. Theoretically, the uniformity index does not have a lower bound – it can be less than zero. The ‘regularized’ uniformity index normalizes uniformity index to range between 0 and 1, with 0 indicating a perfectly *uneven* distribution where only one cluster or perforation gets 100% of the flow (Wehunt et al., 2020).

Initial perforation diameter uncertainty can have a large impact on the uniformity. For example, in the Base Case simulation, 95% of the perforations fall between a 0.34 inch and 0.46 inch initial diameter. With this level of variability, the uniformity indices on a per-shot basis are generally lower (and with a wider spread) than the uniformity indices on a per-cluster basis. The histograms in Figure 9 capture the range of values that could be expected given the uncertainties in perforation phasing, initial perforation diameter, and local tensile strength, as defined in Table 1.

The effect of varying key parameters. Figure 10 shows results from a simulation with settings chosen to generate a toe-bias: (a) no stress shadow from the prior stage, (b) zero ‘gamma’ factor so lateral velocity does

not affect erosion, and (c) no fracture-to-fracture stress shadowing (setting the input parameter ‘fracture net pressure’ to zero). Under these conditions, there is a toe-side bias in proppant placement caused by inertia effects as the proppant flows past the shots (Wu and Sharma, 2016).

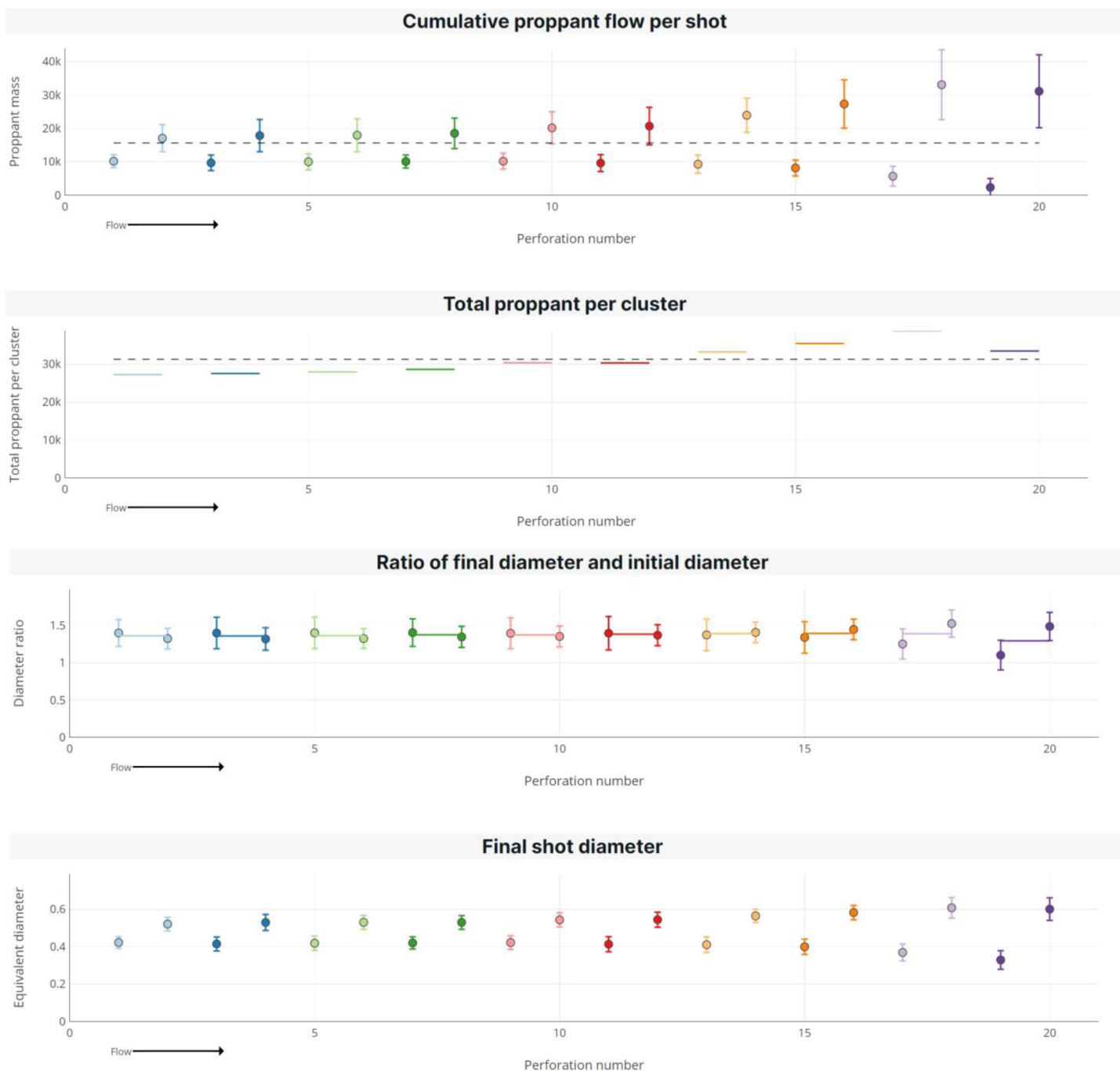


Figure 10—Results from a simulation similar to the Base Case, with the following changes: (a) no stress shadow from the prior stage, (b) zero ‘gamma’ factor so lateral velocity does not affect erosion, and (c) no fracture-to-fracture stress shadowing (net pressure to zero).

Inertial effects are greater with larger diameter particles. As a demonstration, Figure 11 shows results from a calculation that is the same as in Figure 10, except with 30 mesh proppant instead of 100 mesh proppant. The larger diameter proppant results in a stronger toe bias.

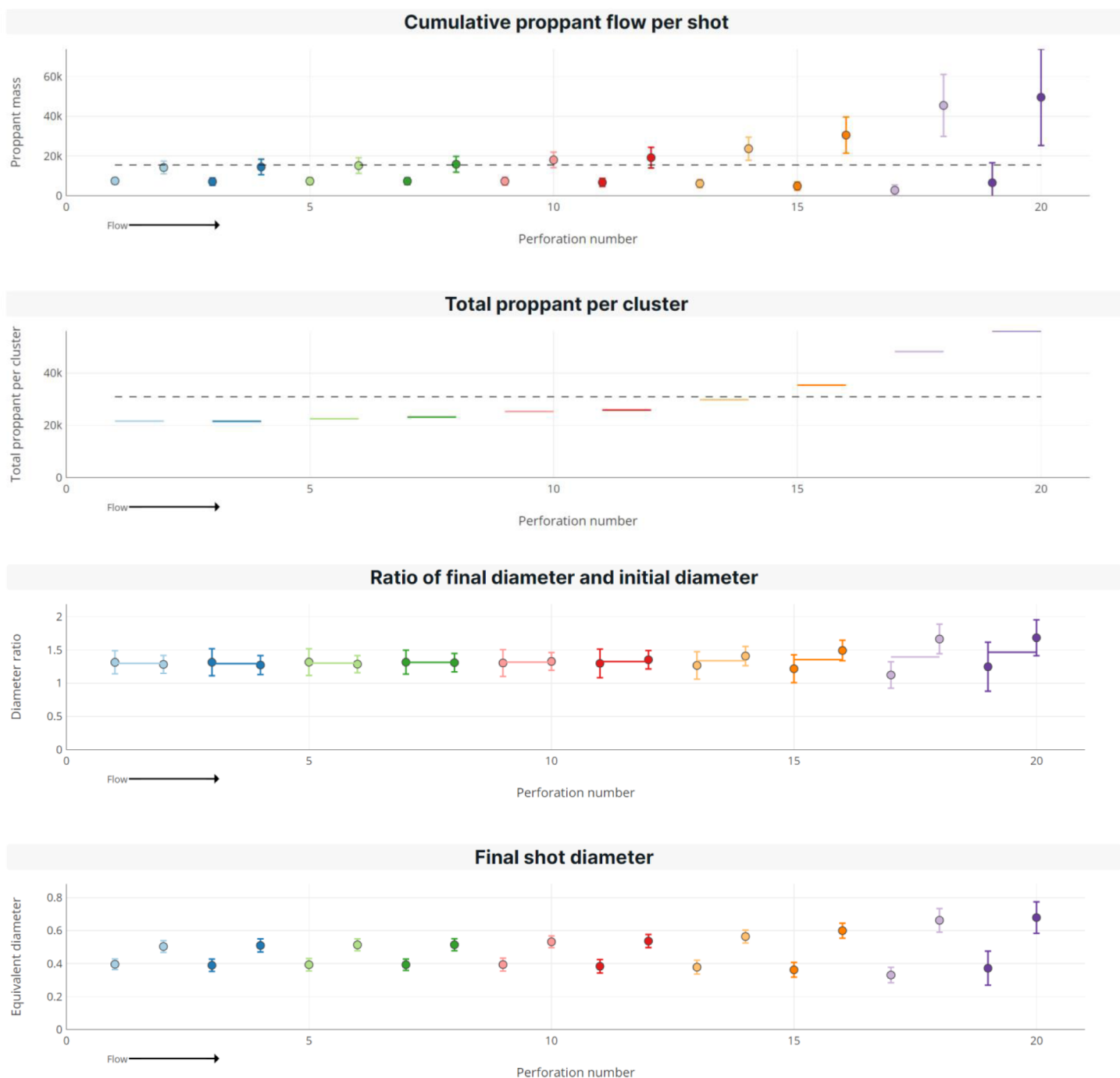


Figure 11—Results from a simulation similar to the Base Case, with the following changes: (a) no stress shadow from the prior stage, (b) zero 'gamma' factor so lateral velocity does not affect erosion, (c) no fracture-to-fracture stress shadowing (net pressure to zero), and (d) 30 mesh proppant (instead of 100 mesh proppant).

Reverting back to the prior settings, [Figure 12](#) shows results from a simulation identical to the Base Case, except a 3x increase in the gamma factor that relates lateral velocity to erosion. Now, we see an even stronger heel bias than in the Base Case.

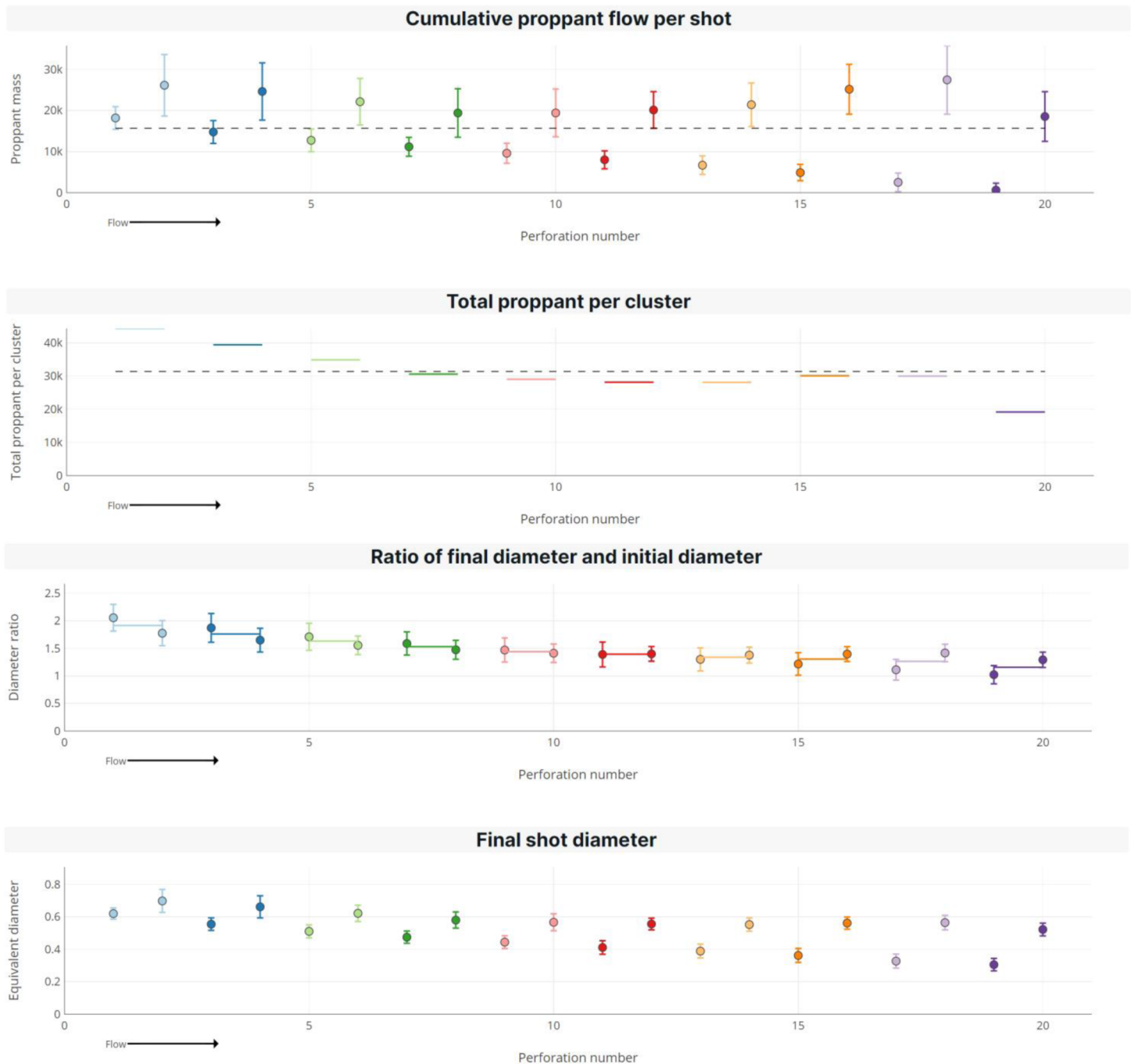


Figure 12—Results from a simulation similar to the Base Case, with the following change: erosion gamma multiplier set to 3.0.

Figure 13 shows a case identical to the Base Case, except with the ‘fracture net pressure’ set to 1000 psi, instead of 200 psi. With such strong stress shadowing between fractures within the stage, flow from the middle section of the stage is discouraged, and there is a U-shaped flow erosion distribution.

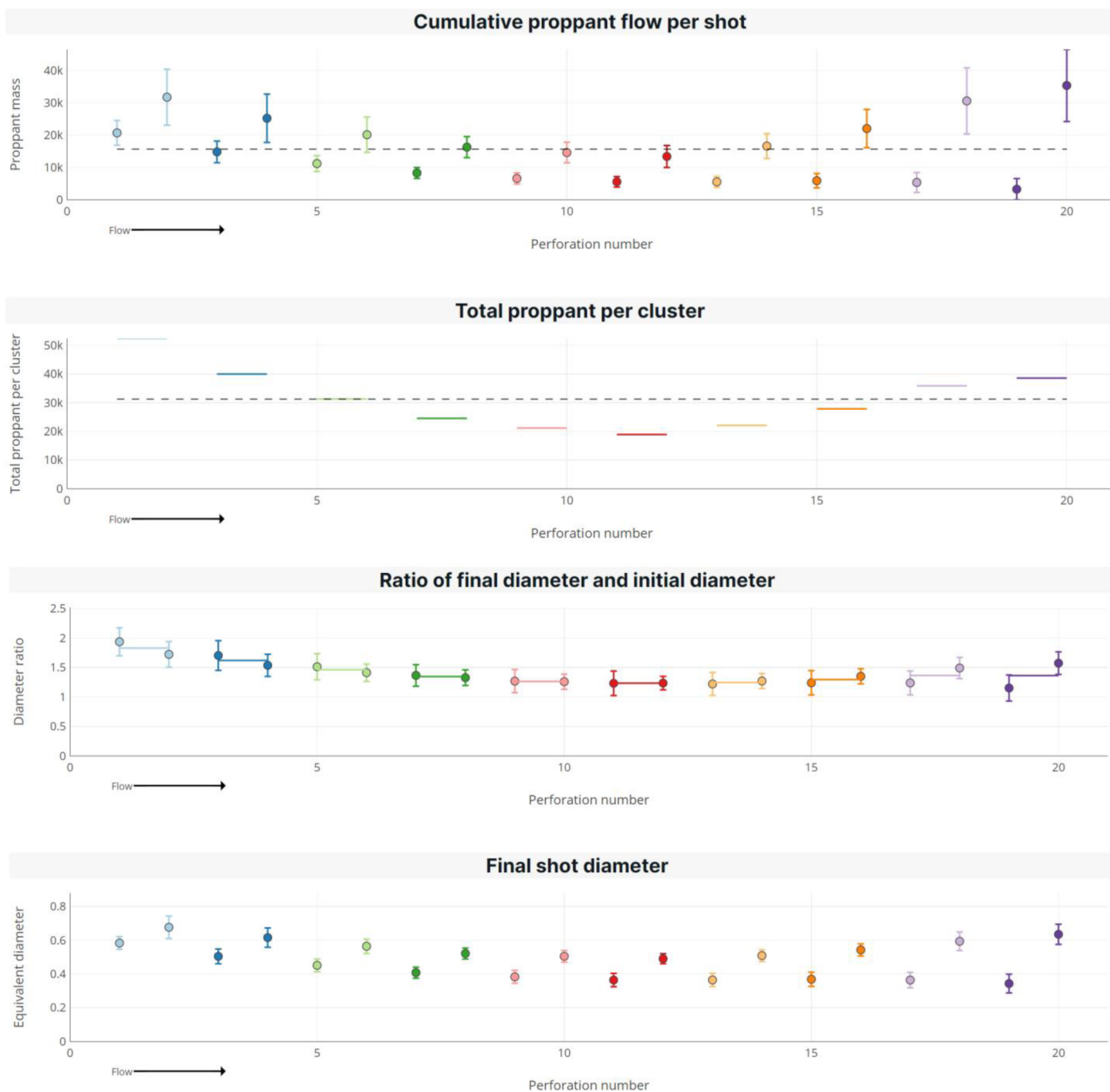


Figure 13—Results from a simulation similar to the Base Case, with the following change: fracture net pressure set to 1000 psi (increased from 200 psi).

Case Study 1

This dataset involves downhole imaging (Robinson et al., 2020) observations of perforation erosion from two wells in the Eagle Ford. The base design used ten perforation clusters in 180 ft stages. Each cluster had three shots, except the two heel-side clusters, which used two shots. The perforation shots within each cluster were at 120° offset from each other, but they were not oriented, and so their phasing within each cluster was random.

Figure 14 shows the distribution of equivalent diameter increase by cluster position, as observed from the downhole imaging. The solid white reference lines show the median of the observed equivalent diameter increase at each cluster. There is a significant heel bias, with erosion in the heel-side clusters significantly greater than erosion in the toe-side clusters.

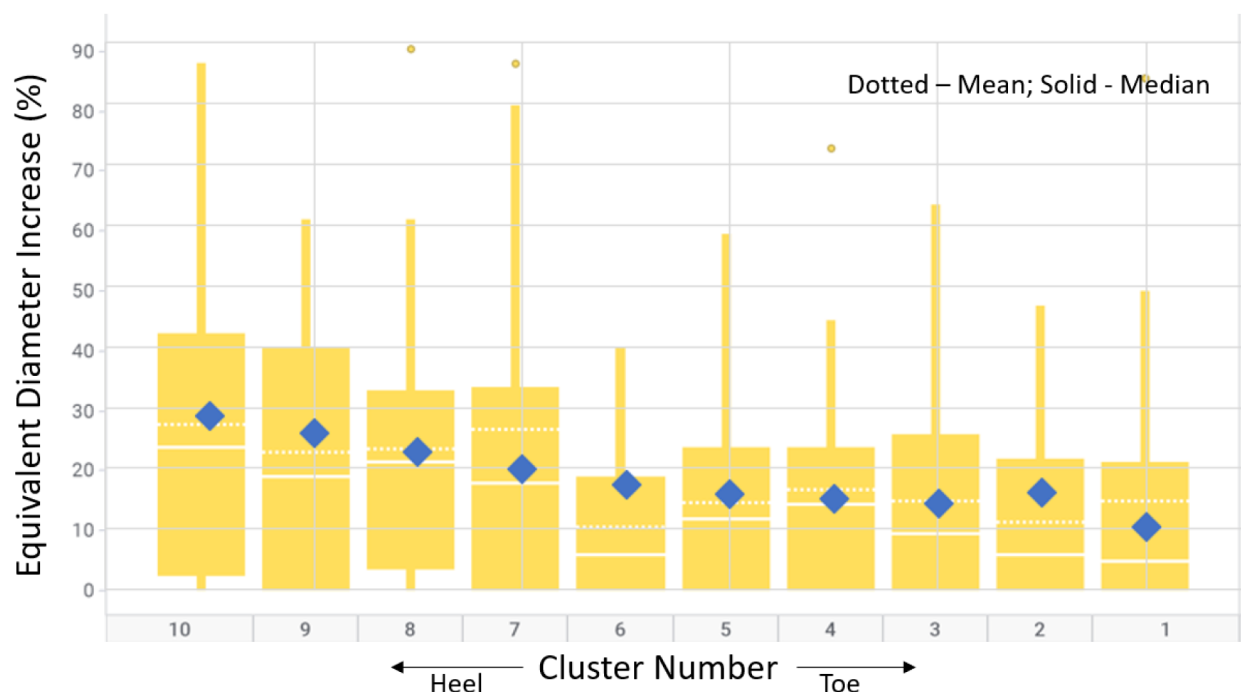


Figure 14—Percent increase in equivalent perforation diameter for the actual data (yellow box and whisker plots) and the simulated data from the calibrated model (blue diamonds) by cluster in Eagle Ford dataset from Case Study 1. Reference lines in the yellow box and whisker plots represent the median (dotted) and mean (solid) of the field data.

Model calibration focused on matching the trend in median diameter increase shown in Figure 14. The match was achieved with the following changes from default parameters – a 20% reduction in the erosion gamma parameter, and a relatively low value for ‘maximum stress shadow from the prior stage’ (300 psi). Random variance in initial diameter and the effect of phasing on initial diameter – inputs to the model – were estimated from calibration shots available in the data.

Figure 15 shows the results from the calibrated simulation model. The predicted erosion (shown in the panel “Ratio of final diameter and initial diameter”) compares favorably with the observations in Figure 14.



Figure 15—Results of the calibrated simulation model for Case Study 1. The ‘Ratio of final diameter and initial diameter’ plot is consistent with the observations shown in Figure 14. Dots correspond to individual shots, while horizontal lines correspond to the average for clusters.

Interestingly, while the simulated erosion distribution has a strong heel bias (the heel-side cluster has about 200% more erosion than the toe-side), the distribution of proppant and slurry is less non-uniform (the heel-side cluster has only about 30% greater flow than the toe-side cluster). This result reinforces that erosion observations cannot be taken as a literal one-to-one measurement of where proppant flowed.

The uniformity index on a per-cluster basis is higher than the uniformity index on a per-shot basis. Because the clusters have two or three shots at 120° phasing, the clusters towards the toe of the stage have large non-uniformity in proppant outflow and erosion between shots *within* each cluster. Generally, towards the toe of the stage, shots at the bottom of the well tend to take more proppant than shots at the top. The shot-to-shot variability within specific stages is evident from the large error bars in slurry outflow shown in Figure 15 for shots towards the toe side of the stage.

Figure 15 shows that the outflow of proppant from the well is fairly uniform on a *per shot* basis. However, the design is tapered so that the two clusters towards the heel have fewer shots. Thus, on a *per cluster* basis, the two tapered clusters take less proppant. The results suggest that uniformity could be improved by using a uniform design, instead of a tapered design.

Sensitivities were run to optimize the magnitude of the perforation pressure drop. Figure 16 shows per-cluster proppant uniformity index for a series of sensitivity analysis simulations varying the magnitude of the perforation pressure drop from very high (far left) to low (far right). Perforation pressure drop was varied by changing the number of shots and/or the initial shot diameter. When limited-entry is excessively low, slurry distribution is dominated by stress shadow; with a large area open to flow, stress shadowing from the prior stage encourages a strong heel bias. On the other hand, we might intuitively expect that designs with the most aggressive perforation pressure drop (fewest shots and smallest perforation diameters) to have the greatest uniformity. This is true for slurry uniformity early in the stage, prior to erosion. However, smaller shot diameter exacerbates: (a) the inertial effects on proppant outflow, and (b) non-uniformity caused by perforation erosion. The optimum design in this case uses a medium amount of limited-entry.

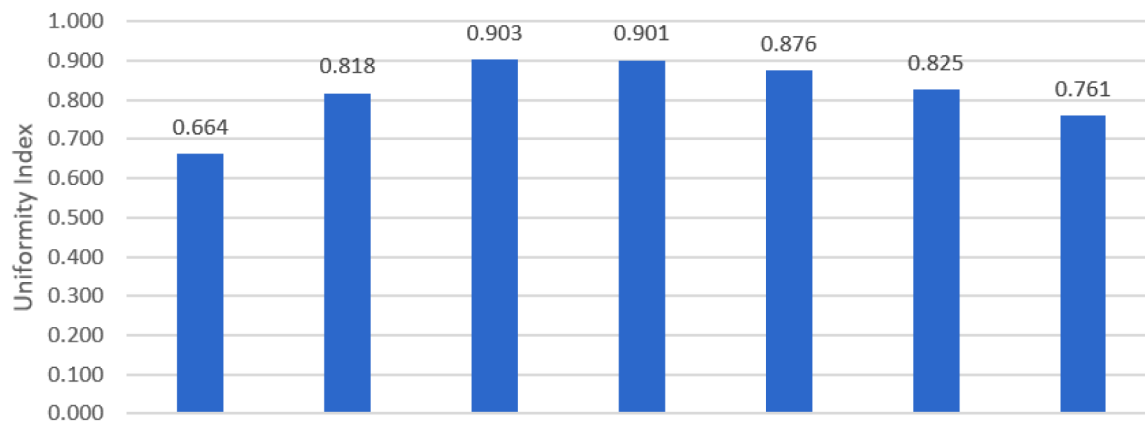


Figure 16—Per-cluster proppant uniformity index for perforating designs with varying amounts of limited-entry. The largest magnitude of limited-entry is shown on the left, with decreasing magnitude from left to right.

Figure 17 shows results from a variety of sensitivities evaluating the effect of perforation phasing, pump schedule, and cluster count. To address operator confidentiality, the details of these sensitivities are not disclosed. The results suggest significant impact on uniformity – either positive or negative – from making changes to the perforation phasing (the three phasing designs considered are shown with the dark blue, light blue, and green bars). Within the range of designs considered, changes to pump schedule and cluster count had a relatively weaker effect (each set of three bars corresponds to one of the designs).

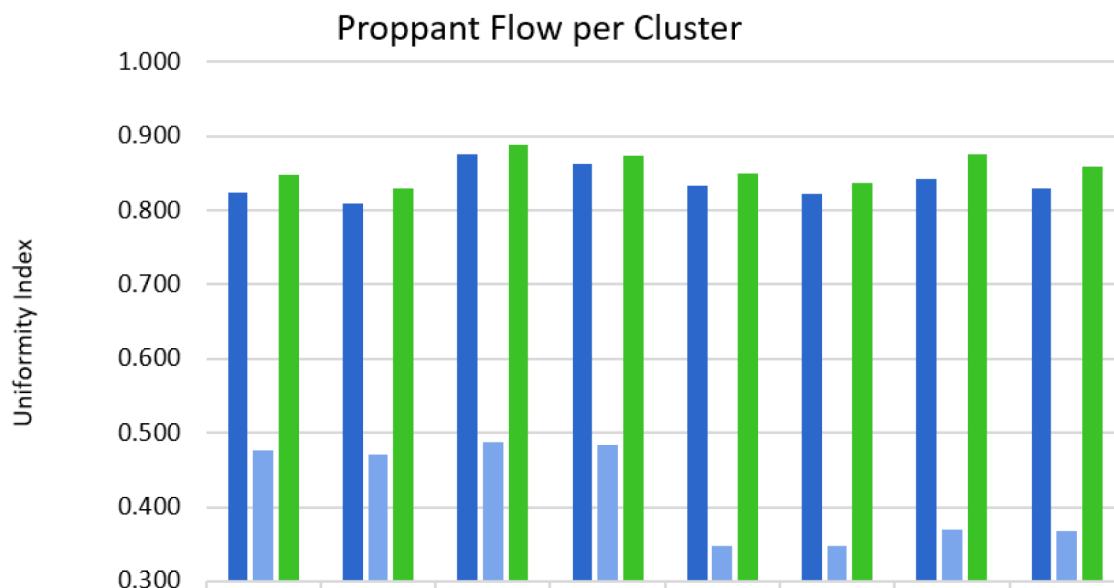


Figure 17—Per-cluster uniformity index for a variety of designs varying perforation phasing, pump schedule, and clusters per stage. To address operator confidentiality, the details of these sensitivities are not disclosed. The dark blue, light blue, and green bars refer to three different choices for perforation phasing. Each group of three bars corresponds to a different fracture design.

Case Study 2

Case Study 2 involved a dataset from the Montney shale play. The operator tested three different designs – Design A with five clusters and wider cluster spacing, Design B with seven clusters and tighter cluster spacing (same stage length as Design A), and Design C with seven clusters and wider cluster spacing (longer stage length than Design A). In all cases, the shots were generally oriented towards the upward half of the wellbore.

The same set of input parameters was used to simultaneously match the data from all three designs. The stage-level and perf-level uncertainty in phasing and the perf-level uncertainty in diameter was estimated directly from the data.

Comparing Figure 14 and Figure 18, it is evident that the dataset in Case Study 2 exhibited significantly more erosion than the dataset in Case Study 1. Consequently, the match in Case Study 2 required a relatively higher value for the erosion ‘alpha’ parameter and a relatively lower value for the erosion ‘gamma’ parameter, compared with Case Study 1. The match in Case Study 2 assumed moderately stronger stress shadow from the prior stage than the match from Case Study 1.

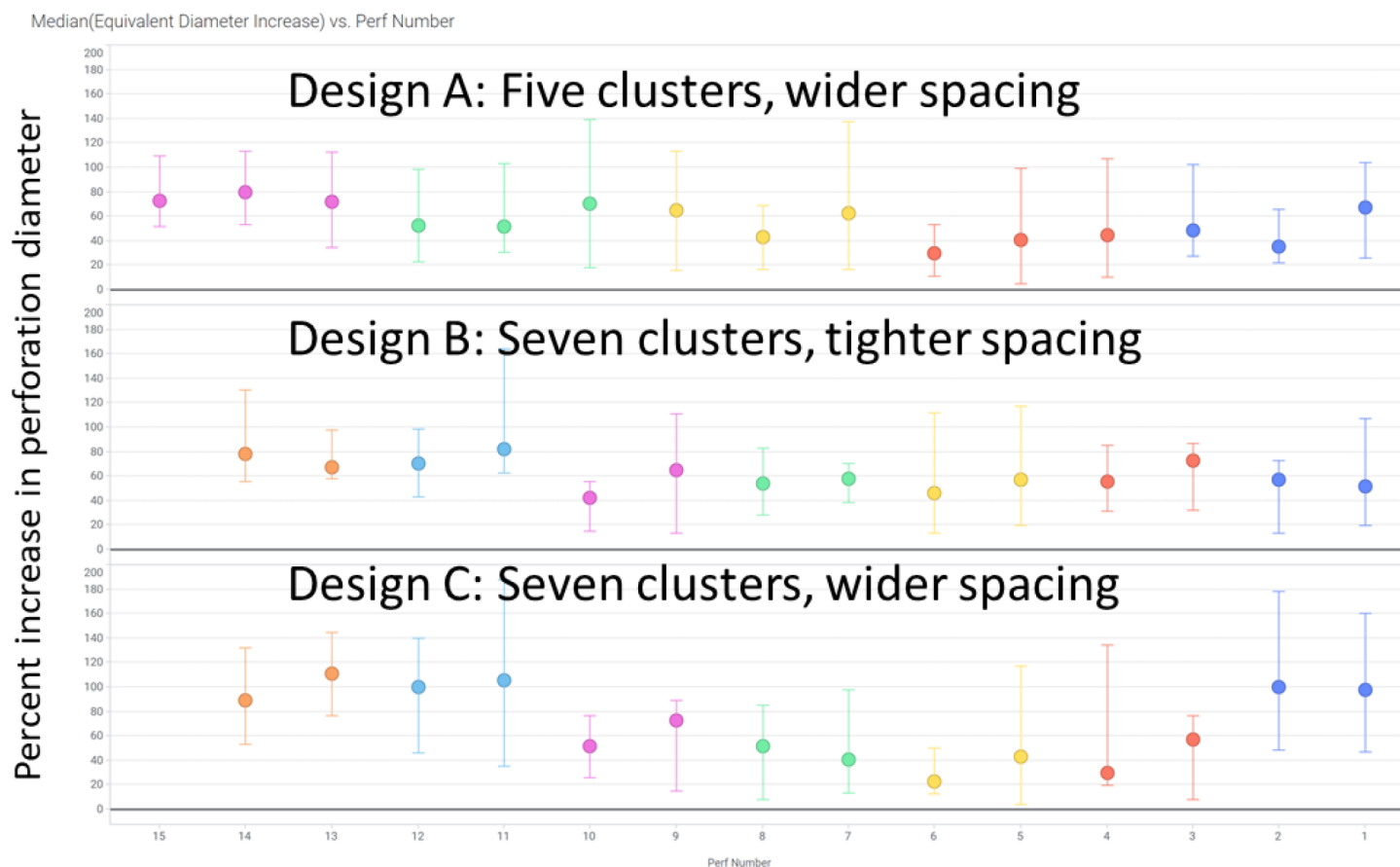


Figure 18—Median percentage increase in ‘equivalent diameter’ of each shot for the three designs in Case Study 2. The dots are colored by cluster number. Error bars represent P10 to P90 ranges. Flow is occurring from left to right.

Figure 19 compares the actual data and the simulated data from the calibrated model. There is greater erosion at the heel, gradually decreasing erosion towards the toe, and then (with Designs A and C) a significant increase in erosion at the final cluster. This trend is consistent with the prediction of the simulator. The increase in proppant outflow at the final cluster occurs because of the gravitational effect as proppant settles downward towards the toe of the stage. The perforations are located along the top of the wellbore, and so the proppant tends to miss the upper perforations as it concentrates towards the bottom as it approaches the toe-side. Because of the relatively low proppant concentration in the slurry outflowing from the middle clusters, the proppant concentration increases gradually as the slurry moves towards the toe side of the stage. At the final cluster, all remaining fluid and proppant must flow out of the well; therefore, the elevated proppant concentration causes a spike in proppant outflow and erosion. Unlike Designs A and C, the data did not show an increase in erosion at the toe cluster with Design B. This may have been due to sample size (random variance), or it may have been caused by greater stress shadowing from the tighter spacing.

An optimization algorithm was used to find the optimal perforation phasing to maximize uniformity of proppant per cluster. The results are shown in Figure 20. With all three designs, the proppant uniformity can be significantly improved with changes to the perforation phasing. In contrast, the slurry uniformity is not as significantly affected by phasing.



Figure 19—Percent increase in equivalent perforation diameter for the actual data (box and whisker plots) and the simulated data from the calibrated model (dots) for Case Study 2. Flow is occurring from left to right.

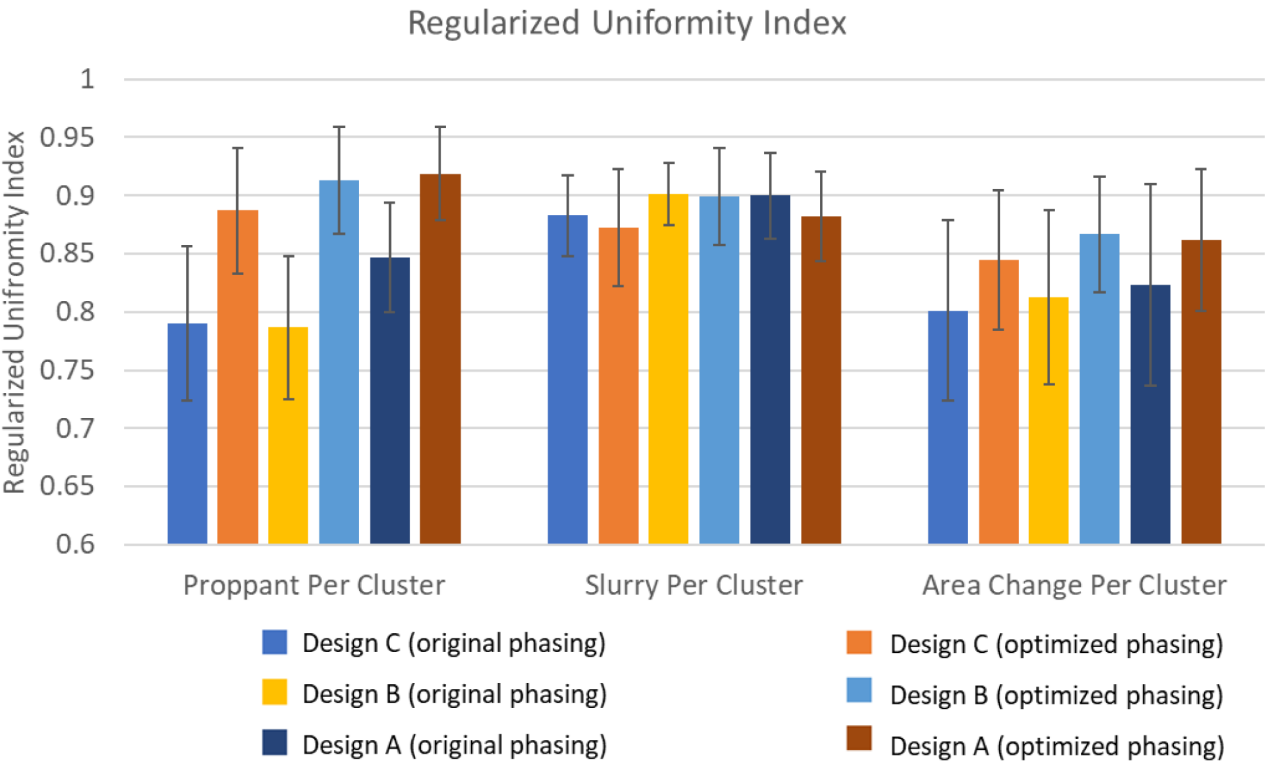


Figure 20—Comparison of the regularized uniformity index with the original perforation phasing and with an optimized phasing.

Random variance in the observed data

The model calibrations in Case Studies 1 and 2 are successful at matching the magnitudes and trends in the median perforation erosion by shot. However, comparison of the error bars in [Figure 14](#), [Figure 15](#), and [Figure 19](#) indicate that the history matches did not fully capture the magnitude of variability in the results from stage to stage. This suggests that the model is missing one or more major sources of random variance in the real data.

The model captures random variability from: (a) perforation phasing, (b) initial perforation diameter, (c) breakdown pressure (effective tensile strength), and (d) random perforation plugging. In ongoing work, we are exploring hypotheses to explain what could cause additional random variability. Additional sources of random variance may include: (a) near-wellbore tortuosity, (b) stress along the lateral, (c) the perforation erosion coefficient, and (d) the proppant mesh size.

Conclusions

The [Dontsov \(2023\)](#) correlation synthesizes physics-based derivations and observations from the literature to predict proppant outflow from the wellbore. In this paper, we integrate the correlation into a wellbore dynamics simulator and calibrate against actual field observations of proppant erosion from case studies in the Eagle Ford and Montney. The workflow enables practical optimization of perforation count, phasing, and diameter to maximize the uniformity of proppant and slurry placement, and ultimately, maximization of recovery factor and project economics.

Key findings include:

- Proppant inertia reduces proppant outflow from the well on the heel side of the stage. This might be expected to cause toe bias in proppant placement. However, a variety of other effects also influence proppant outflow, and as a result, toe bias is not the most common observation in downhole imaging.
- Heel bias in erosion arises from two effects: (a) greater slurry velocity on the heel side of the stage, which exacerbates erosion, and (b) stress shadow from the prior stage. Because of the effect from lateral velocity, heel bias in erosion does not necessarily imply heel bias in proppant placement.
- Some datasets with heel bias exhibit a spike in erosion in the final cluster. This pattern is more likely to occur when shots are placed along the top side of the well. As slurry velocity decreases towards the toe side of the stage, proppant tends to concentrate towards the bottom of the wellbore, and preferentially bypasses the top-side shots. As a result, proppant concentrates towards the toe, and when all slurry must exit the well at the final cluster, there is a spike in erosion.
- Some datasets exhibit a tendency for greater erosion on both the toe and heel sides, with the least erosion within the middle of the stage. In addition to the processes mentioned above, stress shadowing between fractures within the stage contributes to this effect. Intra-stage stress shadowing is greatest in the middle of the stage and is capable of causing a U shaped erosion profile.
- There are meaningful differences in erosion magnitude and trend between field datasets. These differences can be matched with the wellbore dynamics simulator by calibrating a small number of model parameters. Downhole imaging technologies provide a practical and reliable source of data for model calibration.
- The uniformity of proppant placement can be improved by optimizing perforation phasing, diameter, and shot count. These changes are simple and cheap to implement, making perforation design a ‘low hanging fruit’ for improving project economics.

Acknowledgements

We gratefully acknowledge the contributions of two operators who provided the data for the case studies for this paper. Case Study 1 was provided by an anonymous operator. Case Study 2 was provided by Arc Resources. We appreciate the collaboration with colleagues with Arc Resources, including Justin Kitchen, Mani Mehrok, Pierce Anderson, and Farhan Alimahomed. Thank you to the session chair Terry Palisch for the helpful feedback on the manuscript.

Nomenclature

A	= equivalent perforation shot area, in ² or m ²
A_{NW}	= near-wellbore pressure drop coefficient, psi/bpm ^(exponent)
C	= proppant concentration, lbs/gal or kg/m ³
C_d	= discharge coefficient, unitless
$C_{d,max}$	= maximum possible discharge coefficient, unitless
D	= diameter, inches or m
D_{cir}	= circumferential perforation diameter, inches or m
D_{ax}	= axial perforation diameter, inches or m
D_{eq}	= equivalent perforation diameter, inches or m
D_u	= effective perforation shot diameter in the upstream direction, inches or m
D_s	= effective perforation shot diameter in the direction perpendicular to flow, inches or m
D_d	= effective perforation shot diameter in the downstream, inches or m
d_{gun}	= diameter of the perforation gun, inches or m
d_{well}	= diameter of the perforation gun, inches or m
f_D	= pipe friction factor, unitless
G	= dimensionless gravity, unitless
g	= gravitational constant, 9.81 m/s ²
m_p	= total proppant mass, lbs or kg
N	= quantity of either perforation shots or clusters used in calculating regularized uniformity index, unitless
n	= near-wellbore pressure drop exponent, unitless
P_w	= pressure in the wellbore, psi
q_0	= total injection rate, bpm
q_c	= injection rate at a cluster, bpm
$T_{str,eff}$	= effective tensile strength at a perforation cluster, psi
U	= uniformity index for proppant or slurry, unitless
V_s	= total slurry volume, bbl, ft ³ , or m ³
v_p	= lateral superficial velocity through a perforation shot, ft/s or m/s
v_w	= lateral superficial velocity in the well, ft/s or m/s
α	= perforation diameter erosion fitting parameter, in ² -sec/lbs or m ² -s/kg
β	= perforation coefficient of discharge erosion fitting parameter, in-sec/lbs or m-s/kg
γ	= perforation erosion fitting parameter related to lateral velocity, unitless
$\Delta\sigma_e$	= stress shadow at a perforation cluster from the prior stage, psi
$\Delta\sigma_i$	= stress shadow at a perforation cluster from other fractures within the same stage, psi
Δp_{NW}	= near-wellbore pressure drop across a cluster, psi
Δp_p	= perforation pressure drop across a cluster or shot, psi
ρ_f	= fluid density, lbs/gal or kg/m ³
ρ_f	= proppant grain density, lbs/gal or kg/m ³

- ϕ_m = maximum flowing volume fraction of particles, unitless
 σ_{init} = initial magnitude of the minimum principal stress at a cluster, psi
 θ_{gun} = perforation shot phasing from center of the gun, degrees
 θ_{well} = perforation shot phasing from center of the well, degrees
 θ_w = wellbore dip angle, degrees

References

- Ahmad, F.A., and Miskimins, J.L. 2019a. Proppant transport and behavior in horizontal wellbores using low viscosity fluids. In Proceedings of the Hydraulic Fracturing Technology Conference and Exhibition, Houston, TX, SPE-194379-MS.
- Ahmad, F.A. and Miskimins, J.L. 2019b. An experimental investigation of proppant transport in high loading friction-reduced systems utilizing a horizontal wellbore apparatus. In Proceedings of the Unconventional Resources Technology Conference, Denver, CO, URTEC-2019-414-MS.
- Ahmad, F. 2020. Experimental investigation of proppant transport and behavior in horizontal wellbores using low viscosity fluids. PhD thesis, Colorado School of Mines, 2020.
- Ahmad, F.A., Miskimins, J.L., Liu, X., Singh, A., and Wang, J. 2021. Experimental investigation of proppant placement in multiple perforation clusters for horizontal fracturing applications. In Proceedings of the Unconventional Resources Technology Conference, Houston, TX, URTEC-2021-5298-MS.
- Bell, W. T, Sukup R. A., Taruq, S.M. 1987. Perforating. *SPE Monograph Series*, Vol. **16**. ISBN: 978-1-55563-059-1.
- Cramer, D.D. 1987. The Application of Limited-Entry Techniques in Massive Hydraulic Fracturing Treatments. In Proceedings of the SPE Production Operations Symposium, Oklahoma City, OK, SPE-16189-MS.
- Cramer, D., Frieauf, K., Roberts, G., and Whittaker, J. 2020. Integrating distributed acoustic sensing, treatment-pressure analysis, and video-based perforation imaging to evaluate limited-entry-treatment effectiveness. *SPE Prod & Oper*, **35**: 0730–0755, SPE-194334-PA.
- Crump, J.B., and Conway, M.W. 1988. Effects of perforation-entry friction on bottomhole treating analysis. *Journal of Petroleum Technology*, **40**: 1041–1048, SPE-15474-PA.
- Dohmen, T., J.Zhang and J.P.Blangy. 2014. Measurement and analysis of 3D stress shadowing related to the spacing of hydraulic fracturing in unconventional reservoirs. In Proceedings of the Annual Technical Conference and Exhibition, Amsterdam, The Netherlands, SPE-170924-MS.
- Dhulhoya, Karan, and Kyle Frieauf. 2022. Applications of distributed strain sensing via Rayleigh frequency shift: Illuminating near-well and far-field fracture characteristics. In Proceedings of the Unconventional Resources Technology Conference, Houston, TX, URTEC-3721749.
- Dontsov, E., Suarez-Rivera, R. 2020. Propagation of multiple hydraulic fractures in different regimes. *Int J Rock Mech Min Sci*, **128**:104270.
- Dontsov, E.V. 2023. A model for proppant dynamics in a perforated wellbore. *Int. J. Multiph. Flow*, **167**:104552.
- Dontsov, E., Hewson, C., and McClure, M. 2023a. A model for optimizing proppant distribution between perforations. In Proceedings of the American Rock Mechanics Association Symposium, Atlanta, GA.
- Dontsov, E., Hewson, C., and McClure, M. 2023b. Analysis of uniformity of proppant distribution between clusters based on the proppant wellbore dynamics model. In Proceedings of the Unconventional Resources Technology Conference, Houston, TX, URTEC-3854538-MS.
- Gillies, R.G. 1993. Pipeline flow of coarse particle slurries. PhD thesis, University of Saskatchewan.
- Gruesbeck, C. and Collins, R. E. 1982. Particle transport through perforations. *Society of Petroleum Engineers Journal*, **22** (06): 857–865.
- Kaufman, Peter, Mark McClure, Nick Franciose, Sean Owens, Fabiano Srur, and David Russell. Optimizing completions in tank style development. 2019. In Proceedings of the Unconventional Resources Technology Conference, Denver, CO, URTEC-2019-608.
- Lecampion, B., J.Desroches, X.Weng, J.Burghardt and J. E.Brown. 2015. Can we engineer better multistage horizontal completions? Evidence of the importance of near-wellbore fracture geometry from theory, lab and field experiments. In Proceedings of the SPE Hydraulic Fracturing Technology Conference and Exhibition, The Woodlands, TX, SPE-173363-MS.
- Liu, X., Wang, J., Singh, A., Rijken, M., Wehunt, D., Chrusch, L., Ahmad, F., and Miskimins, J. 2021. Achieving near-uniform fluid and proppant placement in multistage fractured horizontal wells: A computational fluid dynamics modeling approach. *SPE Production & Operations*, **36**: 926–945.
- Long, G., Liu, S., Xu, G., and Wong, S.-W. 2015. Modeling of perforation erosion for hydraulic fracturing applications. In Proceedings of the SPE Annual Technical Conference and Exhibition held in Houston, Texas, SPE-174959-MS.

- Lorwongngam, Apiwat (Ohm), Shawn Wright, Stephanie Hari, Erin Butler, Michael McKimmy, Jennifer Wolters, and Craig Cipolla. 2020. Using multidisciplinary data gathering to evaluate eXterme limited entry completion design and improve perforation cluster efficiency. In Proceedings of the Unconventional Resources Technology Conference and Exhibition, Austin, TX, URTEC-2796.
- McClure, Mark. Matteo Picone, Garrett Fowler, Dave Ratcliff, Charles Kang, Soma Medam, and Joe Frantz. 2020. Nuances and frequently asked questions in field-scale hydraulic fracture modeling. In Proceedings of the SPE Hydraulic Fracturing Technology Conference and Exhibition, The Woodlands, TX, SPE-199726-MS.
- McClure, Mark, M.L.Albrecht, C.Bernet, C.L.Cipolla, K.Etcheverry, G.Fowler, A.Fuhr, A.Gherabati, M.Johnston, P.Kaufman, M.Mackay, M.P.McKimmy, C.Miranda, C.Molina, C.G.Ponners, D.R.Ratcliff, J.Rondon, A.Singh, R.Sinha, A.Sung, J.Xu, J.Yeo, R.B.Zinselmeyer. 2023a. Results From a Collaborative Industry Study on Parent/Child Interactions. In Proceedings of the Hydraulic Fracturing Technology Conference and Exhibition, The Woodlands, TX, SPE-212321-MS.
- McClure, Mark, Charles Kang, Chris Hewson, Soma Medam, Egor Dontsov, and Ankush Singh. 2023b. *ResFrac Technical Writeup*. 14th Edition. arXiv:1804.02092.
- Mientka, Matthew, Eric Romberg, and Ellen Scott. 2018. A novel approach to predicting improvements in perforation cluster treatment efficiency. In Proceedings of the SPE International Hydraulic Fracturing Technology Conference and Exhibition, Muscat, Oman, SPE-191467-18IHFT-MS.
- Ngameni, K. L., Miskimins, J. L., Abass H. H., and Cherrian, B. 2017. Experimental study of proppant transport in horizontal wellbore using fresh water. In Proceedings of the Hydraulic Fracturing Technology Conference and Exhibition, The Woodlands, TX, SPE-184841-MS.
- Rateman, Kevin T., Yongshe Liu, and Logan Warren. 2019. Analysis of a drained rock volume: An Eagle Ford example. In Proceedings of the Unconventional Resources Technology Conference, Denver, CO, URTEC-2019-263.
- Robinson, Stephen, Thomas Littleford, Tim Luu, Kacper Wardynski, and rew Evans, Blake Horton, and Michael Oman. 2020. Acoustic imaging of perforation erosion in hydraulically fractured wells for optimizing cluster efficiency. In Proceedings of the SPE Hydraulic Fracturing Technology Conference and Exhibition, The Woodlands, TX, SPE-199718-MS.
- Snider, P., Baumgartner, S., Mayerhofer, M., and Woltz, M. 2022. Execution and learnings from the first two surface tests replicating unconventional fracturing and proppant transport. In Proceedings of the Hydraulic Fracturing Technology Conference, The Woodlands, TX, SPE-209141-MS.
- Xiong, Hongjie. 2020. The effective cluster spacing plays the vital role in unconventional reservoir development – Permian Basin case studies. In Proceedings of the Hydraulic Fracturing Conference and Exhibition, The Woodlands, TX, SPE-199721-MS.
- Wang, J., Singh, A., Liu, X., Rijken, M., Tan, Y., and Naik, S. 2022. Efficient prediction of proppant placement along a horizontal fracturing stage for perforation design optimization. *SPE Journal*, **27**: 1094–1108.
- Weddle, Paul, Larry Griffin, and C. Mark Pearson. 2018. Mining the Bakken II – Pushing the envelope with extreme limited entry perforating. In Proceedings of the SPE Hydraulic Fracturing Technology Conference and Exhibition, The Woodlands, TX, SPE-189880-MS.
- Wehunt, C. D., Naik, S., and Singh, A. 2020. More bang for the buck - optimized perforating design for unconventional reservoirs. In Proceedings of the Hydraulic Fracturing Technology Conference and Exhibition, The Woodlands, TX, SPE-199730-MS.
- Wu, C.-H. and Sharma, M.M. 2016. Effect of perforation geometry and orientation on proppant placement in perforation clusters in a horizontal well. In Proceedings of the Hydraulic Fracturing Technology Conference, The Woodlands, TX, SPE-179117-MS.
- Wu, C. 2018. Modeling Particulate Flows in Conduits and Porous Media. PhD thesis, University of Texas at Austin, Austin, TX.
- Wu, C.-H. and Sharma, M.M. 2019. Modeling proppant transport through perforations in a horizontal wellbore. *SPE Journal*, **2**: 1777–1789, SPE-179117-PA.